Journal of Computational Physics 229 (2010) 6270–6299

Contents lists available at ScienceDirect

Journal of Computational Physics

journal homepage: www.elsevier.com/locate/jcp

On stable parametric finite element methods for the Stefan problem and the Mullins–Sekerka problem with applications to dendritic growth

John W. Barrett [a], Harald Garcke [b], Robert Nürnberg [a,*]

[a] Department of Mathematics, Imperial College London, London SW7 2AZ, UK
[b] NWF I, Mathematik, Universität Regensburg, 93040 Regensburg, Germany

ARTICLE INFO

Article history:
Received 14 September 2009
Accepted 23 April 2010
Available online 7 May 2010

Keywords:
Stefan problem
Mullins–Sekerka problem
Surface tension
Anisotropy
Kinetic undercooling
Gibbs–Thomson law
Dendritic growth
Snow crystal growth
Parametric finite elements

ABSTRACT

We introduce a parametric finite element approximation for the Stefan problem with the Gibbs–Thomson law and kinetic undercooling, which mimics the underlying energy structure of the problem. The proposed method is also applicable to certain quasi-stationary variants, such as the Mullins–Sekerka problem. In addition, fully anisotropic energies are easily handled. The approximation has good mesh properties, leading to a well-conditioned discretization, even in three space dimensions. Several numerical computations, including for dendritic growth and for snow crystal growth, are presented.

1. Introduction

Pattern formation resulting from the motion of a two-phase boundary in a diffusing field appears in many physical situations, such as the growth of snowflakes, solidification of metals and Ostwald ripening in alloys. Often a dendritic structure appears during the growth of crystals leading to complex forms with side branches, as can be seen for snow crystals and for dendrites of a solidifying alloy. It is by now well understood that surface energy effects are important in these pattern forming scenarios. Roughly speaking, patterns emerge in diffusive driven phase boundary motion via the competition between interface energy and diffusion. To keep the interface energy small, the (weighted) surface area has to be small. On the other hand, the diffusion kinetics prefer to drive the system into irregular shapes with large surface area so that, e.g. in solidification, latent heat can diffuse away from the solidifying front more easily. We refer to the review [15], the book [20] and the references therein for more information on the physics of pattern formation in diffusive systems.

Patterns arise in diffusive phase boundary motion since a growing front becomes unstable. A meaningful attempt to numerically approximate these phenomena should make sure that the numerical method used does not lead to additional instabilities, and hence to patterns which result from the discretization. It is by now well accepted that some of the first numerical results on pattern forming systems led to patterns which resulted from numerical errors. For example, often side branches in dendritic growth simulations disappear when the grid parameters are sufficiently refined, see e.g. [51, Fig. 4.5].

* Corresponding author. Tel.: +44 020 759 48572.
E-mail addresses: j.barrett@imperial.ac.uk (J.W. Barrett), harald.garcke@mathematik.uni-regensburg.de (H. Garcke), robert.nurnberg@imperial.ac.uk (R. Nürnberg).

0021-9991/$ - see front matter © 2010 Elsevier Inc. All rights reserved.
doi:10.1016/j.jcp.2010.04.039

Taking the unstable behaviour of the process into account, it is important to come up with a numerical method that is stable in the sense that dissipation inequalities which are true for the continuous problem have a natural discrete analogue. If this is guaranteed, one reduces the likelihood that instabilities are triggered by the numerical method.

It is the goal of this paper to introduce such a discretization for the free boundary problem which governs the evolution of phase boundary motion in diffusive systems. For dendritic growth it is also important to take the anisotropic nature of surface energy into account. Based on earlier work by the authors, see [9], our presented numerical method is able to handle fully anisotropic situations, which is particularly challenging as here the underlying equations are highly nonlinear.

The governing equations for the two-phase boundary motion, that we consider, are diffusion equations in the bulk coupled to the Stefan condition on the free boundary, which requires heat conservation on the phase boundary. In addition, one requires a condition stating local thermodynamical equilibrium on the two-phase interface. This condition is given by the Gibbs–Thomson relation with kinetic undercooling in which, typically, one has to allow for anisotropy. The full problem, that we consider, goes back to [45] and [60], the latter being the translation of [59]. We note that for a fully anisotropic situation, Gurtin derived the governing system within the context of rational thermodynamics in [34]. For reviews we refer to [39,35,58,20]. An important result on the Stefan problem with the Gibbs–Thomson law is the seminal work [45] and [46], where a linear stability analysis was used to show that a growing nucleus and a moving planar front, respectively, become unstable at large undercoolings. It is this instability which is the basic reason for pattern formation in diffusion driven interface motion, in situations where capillary effects cannot be neglected. Snow crystal formation is the most prominent example for such a pattern forming event.

Existence results for the Stefan problem with the Gibbs–Thomson law are were derived in [19] for local-in-time smooth solutions, and in [41] for global-in-time weak solutions. Both results are for isotropic situations, but we mention here that the result in [41] was recently generalized in [31] to anisotropic situations. In many situations the interface evolution is slow compared to the time scale for diffusion in the bulk. Hence, it is often justified to replace the full parabolic diffusion equation in the bulk by a quasi-static diffusion equation, i.e. an elliptic equation has to be solved at each instance in time. The resulting system is the Mullins–Sekerka problem, and we refer to [24,27] for a local well-posedness result, and to [42,48] for results on global-in-time weak solutions.

Mathematical approaches for the numerical approximation of the Stefan problem can be distinguished according to how the two-phase interface is treated. Apart from parametric or front-tracking approaches, such as the one considered in this paper, there exist phase field and level set methods. We remark that over the last two decades phase field methods, in particular, have been successfully used to model crystal growth and other related phenomena. In phase field methods the sharp interface is replaced by a diffuse interfacial layer for an order parameter. For the numerical simulation of dendritic growth in three dimensions, this method was first used in [38]. We refer to [16,18,55] for recent review articles. A similar idea is used for level set methods. Here the sharp interface is represented as the zero level set of an auxiliary function, the so called level set function, the evolution of which is described by a highly nonlinear PDE, which can be solved on e.g. a fixed Cartesian grid. We refer to the books [54,47] and the paper [29] for more details.

In this paper we will consider a parametric approach. Alternative sharp interface approaches for the Stefan problem with the Gibbs–Thomson law, where the interface is tracked explicitly, have been used and proposed in e.g. [1,50,49,51,37,52]. We mention here, in particular, the pioneering work [50,51], where for the first time the full Stefan problem in three dimensions was solved within a sharp interface framework. Together with [38], these constitute the first numerical simulations of dendritic growth in 3d in the literature. We remark that our approach has some similarities to the approach by Schmidt, which is based on the coupling of a finite element method for solving the diffusion equation in the bulk to a parametric finite element method for the evolution of the two-phase interface. The latter makes use of ideas in [25], which allow the computation of a discrete mean curvature vector of a polyhedral surface in a variational context. Compared to [51] our approach has the advantages that (a) fully anisotropic surface energies can be treated, (b) it mimics the Lyapunov structure for the continuous problem in both the isotropic and anisotropic case, and (c) no smoothing of the interface mesh is needed in practice. In addition, we can also handle quasi-static variants, such as the Mullins–Sekerka problem, which play an important role in practice.

For numerical approaches to the Mullins–Sekerka problem we refer to [14,62,44,13], where the approximations are based on a boundary integral formulation. In the paper [62] a method, which was introduced in [36] for the equidistribution of mesh points on evolving planar curves, is used in order to remove the "stiffness" introduced through the curvature term. We remark that our approach also removes the "stiffness" of interfacial evolution problems as our method has very good properties with respect to the grid spacing, leading to a well-conditioned discretization. We refer to [6,8] for a discussion of mesh properties in our approach; and remark that, in contrast to the approach of [36], our approach can also be applied in three space dimensions.

Let us summarize the advantages of our approximation compared to existing approaches:

- Our fully discrete scheme closely mimics an underlying Lyapunov structure of the continuous problem, leading to an unconditionally stable approximation in certain situations. Moreover, a semidiscrete version of our scheme is always stable and, in addition, conserves certain physical quantities exactly; see Remark 3.5 below.
- Like most other parametric approaches, we approximate the continuous interface Γ by a polyhedral surface Γ^m. Often in parametric approaches the mesh gets distorted during the time evolution, making a reparameterization or mesh smoothing necessary. Instead, we obtain asymptotic equidistribution in two space dimensions, while in 3d the meshes in general remain well distributed. This, in particular, leads to a well-conditioned discretization.

- It is straightforward to include fully anisotropic surface energies into our model, for both two and three space dimensions. In particular, we consider the Gibbs–Thomson law with an anisotropic mean curvature, as it was derived in [34].
- The cross terms involving the bulk and interface meshes are integrated exactly. This appears sensible, as it is the interaction at the interface which mainly drives the evolution. Most other approaches in the literature use quadrature for simplicity, see e.g. [51], which, in particular, are not exact even for piecewise linear functions in the bulk. However, we remark that exact integration for piecewise linear finite elements has been considered previously, e.g. in [50].
- Quasi-static variants of the Stefan problem, such as the Mullins–Sekerka problem, can be handled naturally in our formulation. For the Mullins–Sekerka problem our numerical discretization has a natural gradient flow structure, which is related to the continuous situation; see the Appendix A for more details.

The remainder of the paper is organized as follows. In Section 2 we state strong and weak formulations of the Stefan problem and the Mullins–Sekerka problem that we consider in this paper. In Section 3 we introduce our numerical approximation for these problems; that is, a coupled finite element approximation for the interface evolution and the diffusion equation in the bulk. Moreover, we will show well-posedness and stability results for our numerical approximations. Solution methods for the discrete equations and mesh adaptation strategies are discussed in Sections 4 and 5, respectively. In addition, we present several numerical experiments, including simulations of snow crystal formations in three space dimensions, in Section 6. Finally, in the Appendix A we present a gradient flow description of our spatially discrete approximation for the Mullins–Sekerka problem.

2. The mathematical models

Let $\Omega \subset \mathbb{R}^d$, $d = 2, 3$, be a domain occupied by a material which at each time t and at each space point $\vec{z} \in \Omega$ is either liquid or solid and let $\vec{\nu}_\Omega$ be the outer unit normal to $\partial\Omega$, the boundary of Ω. The solid–liquid interface is at each time t assumed to be a sufficiently smooth hypersurface $\Gamma(t) \subset \overline{\Omega}$. We assume furthermore that $\Gamma = (\Gamma(t))_{t\in[0,\overline{T}]}$, $\overline{T} > 0$, is a sufficiently smooth evolving hypersurface parameterized by $\vec{x}(\cdot, t) : \Upsilon \to \mathbb{R}^d$, where $\Upsilon \subset \mathbb{R}^d$ is a given reference manifold, i.e. $\Gamma(t) = \vec{x}(\Upsilon, t)$. Moreover, we denote the solid region by $\Omega_s(t)$ and the liquid region is then given as $\Omega_l(t) := \Omega \setminus \overline{\Omega_s(t)}$. Throughout this paper, for a quantity v defined on Ω, we use the shorthand notations $v_s := v|_{\Omega_s}$ and $v_l := v|_{\Omega_l}$. For the interface Γ, we adopt the convention that its unit normal $\vec{\nu}$ points into Ω_l; see Fig. 1. The mean curvature $\varkappa$ of Γ is defined to be the sum of the principal curvatures of Γ and we adopt the sign convention that $\varkappa$ is negative for a convex domain $\Omega_s(t)$. Furthermore, $\mathcal{V} := \vec{x}_t \cdot \vec{\nu}$ is the normal velocity of the evolving hypersurface Γ.

2.1. Strong formulation of the Stefan problem

The Stefan problem with the Gibbs–Thomson law and kinetic undercooling in its anisotropic version is now given as follows. Find $u : \Omega \times [0, \overline{T}] \to \mathbb{R}$ and the interface $(\Gamma(t))_{t\in[0,\overline{T}]}$ such that for all $t \in (0, \overline{T}]$ the following conditions hold:

$$\vartheta u_t - \mathcal{K}_s \Delta u = f_s \quad \text{in } \Omega_s(t), \quad \vartheta u_t - \mathcal{K}_l \Delta u = f_l \quad \text{in } \Omega_l(t), \tag{2.1a}$$

$$\left[\mathcal{K} \frac{\partial u}{\partial \vec{\nu}}\right]_{\Gamma(t)} = -\lambda \mathcal{V} \quad \text{on } \Gamma(t), \tag{2.1b}$$

$$\frac{\rho \mathcal{V}}{\beta(\vec{\nu})} = \alpha \varkappa_\gamma - a u \quad \text{on } \Gamma(t), \tag{2.1c}$$

$$\frac{\partial u}{\partial \vec{\nu}_\Omega} = 0 \quad \text{on } \partial_N\Omega, \quad u = u_D \quad \text{on } \partial_D\Omega, \tag{2.1d}$$

$$\Gamma(0) = \Gamma_0, \quad \vartheta u(\cdot, 0) = \vartheta u_0 \quad \text{in } \Omega; \tag{2.1e}$$

where $[\mathcal{K} \frac{\partial u}{\partial \vec{\nu}}]_{\Gamma(t)}(\vec{z}) := (\mathcal{K}_l \frac{\partial u_l}{\partial \vec{\nu}} - \mathcal{K}_s \frac{\partial u_s}{\partial \vec{\nu}})(\vec{z})$ for all $\vec{z} \in \Gamma(t)$ and $\partial\Omega = \overline{\partial_N\Omega} \cup \overline{\partial_D\Omega}$ with $\partial_N\Omega \cap \partial_D\Omega = \emptyset$. In addition, $\Gamma_0 \subset \overline{\Omega}$ and $u_0 : \Omega \to \mathbb{R}$ are given initial data.

In the above f describes heat sources and $u = T - T_M$ denotes the deviation from the melting temperature, i.e. T_M is the melting temperature for a planar interface and T is the absolute temperature in Kelvin. By ϑ we denote the volumetric heat capacity, and $\mathcal{K}$ is the heat conductivity. Here ϑ is assumed to be constant in Ω, while $\mathcal{K}$ is assumed to be constant in each phase. Moreover, λ is the latent heat per unit volume, α is an interfacial energy density per surface area, ρ is a kinetic coefficient and a is a coefficient having the dimension entropy/volume. All of the above parameters are assumed to be non-negative and we will always assume that $\mathcal{K}, a$ and λ are strictly positive. The quantity $\varkappa_\gamma$ is an anisotropic mean curvature which will be specified later. We only remark that in the isotropic case $\varkappa_\gamma$ reduces to the mean curvature $\varkappa$. In addition, $\beta(\vec{\nu})$ is a dimensionless mobility function which allows one to describe the dependence of the mobility on the local orientation of the interface.

The model (2.1a)–(2.1e) can be derived for example within the theory of rational thermodynamics and we refer to [34] for details. We remark that a derivation from thermodynamics would lead to the identity:

$$a = \frac{\lambda}{T_M}. \tag{2.2}$$

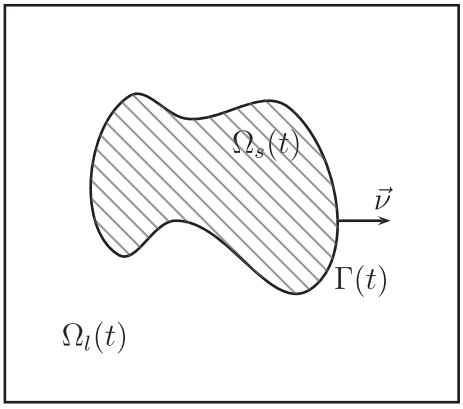

Fig. 1. The domain Ω in the case $d = 2$.

We note that (2.1b) is the well-known Stefan condition, while (2.1c) is the Gibbs–Thomson condition, with kinetic undercooling if $\rho > 0$. The case $\vartheta > 0$, $\rho > 0$, $\alpha > 0$ leads to the Stefan problem with the Gibbs–Thomson law and kinetic undercooling. In some models in the literature, see e.g. [41], the kinetic undercooling is set to zero, i.e. $\rho = 0$. Setting $\vartheta = \rho = 0$ but keeping $\alpha > 0$ leads to the Mullins–Sekerka problem with the Gibbs–Thomson law, see [45]. In situations where the interface $\Gamma(t)$ meets the external boundary $\partial\Omega$, an angle condition needs to be prescribed. We will discuss this issue in more detail in the section on the numerical discretization. We remark that the problem (2.1a)–(2.1e) also appears in solidification from a supersaturated solution, and in this case the problem (2.1a)–(2.1e) includes conservation equations for a concentration, see [15] or [20] for details. This situation is relevant e.g. for the snow crystal simulations in Section 6.

We note that in addition we could consider e.g. the classical Stefan problem ($\vartheta > 0$, $\rho = \alpha = 0$) and its quasi-static variant ($\vartheta = \rho = \alpha = 0$). However, as these problems do not involve curvature, as $\alpha = 0$, they can be easily solved with well established numerical methods such as the enthalpy method and the variational inequality approach after applying the Baiocchi transform, respectively; see e.g. [26]. Hence throughout this paper, we assume that $\alpha > 0$, so that the problem (2.1a)–(2.1e) couples u, $\Gamma(t)$ and $\varkappa_\gamma$.

It now remains to introduce the anisotropic mean curvature $\varkappa_\gamma$. One obtains $\varkappa_\gamma$ as the first variation of an anisotropic interface free energy:

$$|\Gamma|_\gamma := \int_\Gamma \gamma(\vec{\nu})\, ds,$$

where $\gamma : \mathbb{R}^d \to \mathbb{R}_{\geqslant 0}$, with $\gamma(\vec{p}) > 0$ if $\vec{p} \neq \vec{0}$, is the surface free energy density which depends on the local orientation of the surface via the normal $\vec{\nu}$. The function γ is assumed to be positively homogeneous of degree one, i.e.

$$\gamma(b\vec{p}) = b\,\gamma(\vec{p}) \quad \forall\, \vec{p} \in \mathbb{R}^d, \quad \forall\, b > 0 \Rightarrow \gamma'(\vec{p}).\vec{p} = \gamma(\vec{p}) \quad \forall \vec{p} \in \mathbb{R}^d \setminus \{\vec{0}\},$$

where γ' is the gradient of γ. In the isotropic case we have that:

$$\gamma(\vec{p}) = |\vec{p}| \qquad \forall \vec{p} \in \mathbb{R}^d, \tag{2.3}$$

and so $\gamma(\vec{\nu}) = 1$, which means that $|\Gamma|_\gamma$ reduces to $|\Gamma|$, the surface area of Γ. The first variation of $|\Gamma|_\gamma$ is given by, see e.g. [9]:

$$\varkappa_\gamma := -\nabla_s.\gamma'(\vec{\nu});$$

where $\nabla_s.$ is the tangential divergence of Γ, i.e. we have in particular that:

$$\frac{d}{dt}\,|\Gamma(t)|_\gamma = \frac{d}{dt}\int_{\Gamma(t)} \gamma(\vec{\nu})\, ds = -\int_{\Gamma(t)} \varkappa_\gamma\, \mathcal{V}\, ds.$$

A wide class of anisotropies can be modelled by

$$\gamma(\vec{p}) = \left(\sum_{\ell=1}^{L} [\gamma_\ell(\vec{p})]^r\right)^{\frac{1}{r}}, \quad \gamma_\ell(\vec{p}) := [\vec{p}\cdot G_\ell\,\vec{p}]^{\frac{1}{2}}, \tag{2.4}$$

so that:

$$\gamma'(\vec{p}) = [\gamma(\vec{p})]^{1-r} \sum_{\ell=1}^{L} [\gamma_\ell(\vec{p})]^{r-1}\, \gamma'_\ell(\vec{p}),$$

where $r \in [1,\infty)$ and $G_\ell \in \mathbb{R}^{d\times d}$, $\ell = 1 \to L$, are symmetric and positive definite. Our numerical method will be based on anisotropies of the form (2.4). This novel choice of anisotropy was first considered in [7] and [9], and there it enabled the authors

to introduce unconditionally stable fully discrete finite element approximations for the anisotropic mean curvature flow, i.e. (2.1c) with $a = 0$, and other geometric evolution equations for an evolving interface Γ. Similarly, in this paper, the choice of anisotropies (2.4) will lead to fully discrete approximations of (2.1a)–(2.1e) with very good stability properties. We note that the simpler choice $r = 1$, which leads to a finite element approximation with a linear system to solve at each time level, see (3.5a)–(3.5c) below, is sufficient for the case $d = 2$. But in three space dimensions, the choice $r = 1$ leads to only a relatively small class of anisotropies, which is why the authors introduced the more general (2.4) in [9].

We now give some examples for anisotropies of the form (2.4), which later on will be used for the numerical simulations in this paper. For the visualizations we will use the Wulff shape, [61], defined by

$$\mathcal{W} := \{\vec{p} \in \mathbb{R}^d : \vec{p} \cdot \vec{q} \leqslant \gamma(\vec{q}) \quad \forall\, \vec{q} \in \mathbb{R}^d\}. \tag{2.5}$$

Here we recall that the Wulff shape $\mathcal{W}$ is known to be the solution of an isoperimetric problem, i.e. the boundary of $\mathcal{W}$ is the minimizer of $|\cdot|_\gamma$ in the class of all surfaces enclosing the same volume, see e.g. [28].

Let:

$$l^1_\varepsilon(\vec{p}) := \sum_{j=1}^{d} \left[\varepsilon^2 |\vec{p}|^2 + p_j^2 (1-\varepsilon^2)\right]^{\frac{1}{2}} \quad \text{and} \quad l^2_\varepsilon(\vec{p}) := \left[|\vec{p}|^2 - (1-\varepsilon^2) p_d^2\right]^{\frac{1}{2}}, \quad \varepsilon > 0,$$

be a regularized l^1-norm and a regularized $(d-1)$-dimensional l^2-norm, respectively. Then $\gamma(\vec{p}) = l^1_\varepsilon(\vec{p})$ and, for $d = 2$, $\gamma(\vec{p}) = l^1_\varepsilon(R(\frac{\pi}{2})\vec{p})$, where $R(\theta)$ denotes a clockwise rotation through the angle θ, are two examples for (2.4), and their Wulff shapes for $\varepsilon = 0.5$ and $\varepsilon = 0.4$, respectively, are shown in Fig. 2. A hexagonal anisotropy in $\mathbb{R}^2$ can be modelled with the choice $\gamma(\vec{p}) = \sum_{\ell=1}^{3} l^2_\varepsilon(R(\frac{\ell\pi}{3})\vec{p})$, and its Wulff shape for $\varepsilon = 0.01$ is shown on the right of Fig. 2.

In order to define some anisotropies of the form (2.4) in $\mathbb{R}^3$, we introduce the rotation matrices $R_1(\theta) := \begin{pmatrix} \cos\theta & \sin\theta & 0 \\ -\sin\theta & \cos\theta & 0 \\ 0 & 0 & 1 \end{pmatrix}$ and $R_2(\theta) := \begin{pmatrix} \cos\theta & 0 & \sin\theta \\ 0 & 1 & 0 \\ -\sin\theta & 0 & \cos\theta \end{pmatrix}$. Then $\gamma(\vec{p}) = \sum_{\ell=1}^{3} l^2_\varepsilon(R_1(\frac{\ell\pi}{3})\vec{p}) + l^2_\varepsilon(R_2(\frac{\pi}{2})\vec{p})$ is one such example, and its Wulff shape for $\varepsilon = 0.1$ is shown in Fig. 3. Finally, the Wulff shape of

$$\gamma(\vec{p}) = \left(\left[l^2_\varepsilon(\vec{p})\right]^r + \left[l^2_\varepsilon\left(R_1\left(\frac{\pi}{2}\right)\vec{p}\right)\right]^r + \left[l^2_\varepsilon\left(R_2\left(\frac{\pi}{2}\right)\vec{p}\right)\right]^r\right)^{\frac{1}{r}}, \tag{2.6}$$

for $r = 9$ and $\varepsilon = 0.5$ is shown on the right of Fig. 3. We remark that for smaller values of ε and larger values of r, the Wulff shape of (2.6) will approach an octahedron, as can be seen in [9, Fig. 4]. However, for the problems considered in this paper, even a mild anisotropy as depicted in Fig. 3 already leads to very pronounced dendritic growth; see e.g. Section 6.5 below. More examples of anisotropies of the form (2.4) can be found in [7,9,11].

2.2. Weak formulation of the Stefan problem

For later reference, we introduce the function spaces:

$$S_0 := \{\phi \in H^1(\Omega) : \phi = 0 \quad \text{on} \quad \partial_D\Omega\} \quad \text{and} \quad S_D := \{\phi \in H^1(\Omega) : \phi = u_D \quad \text{on} \quad \partial_D\Omega\},$$

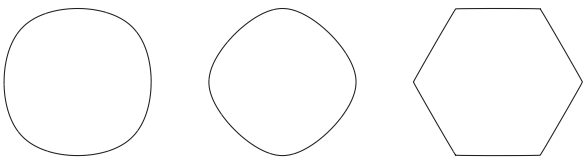

Fig. 2. Wulff shapes for different choices of (2.4) in $\mathbb{R}^2$. Here $L = 2$, 2, 3 and $\varepsilon = 0.5$, 0.4, 0.01.

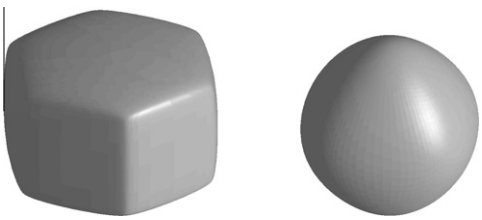

Fig. 3. Wulff shapes for different choices of (2.4) in $\mathbb{R}^3$. Here $L = 4$, $r = 1$ and $\varepsilon = 0.1$ (left); and $L = 3$, $r = 9$ and $\varepsilon = 0.5$ (right).

where we assume for simplicity of the presentation from now on that either:

$$\text{(i) } \partial\Omega = \partial_D\Omega, \quad \text{or} \quad \text{(ii) } \partial\Omega = \partial_N\Omega, \quad \text{or} \quad \text{(iii) } \Omega = (-H,H)^d, \quad \partial_D\Omega = [-H,H]^{d-1}\times\{H\}, \quad H>0; \tag{2.7}$$

and, in the cases (2.7)(i) and (iii), that $u_D \in H^{\frac{1}{2}}(\partial_D\Omega)$. For notational convenience, we define $u_D := 0$ in the case (2.7)(ii). In addition, we define:

$$\underline{V} := H^1(\Upsilon,\mathbb{R}^d) \quad \text{and} \quad W := H^1(\Upsilon,\mathbb{R}),$$

where we recall that Υ is a given reference manifold. A possible weak formulation of (2.1a)–(2.1e), which utilizes the novel weak representation of $\varkappa_\gamma\,\vec{\nu}$ introduced in [9], is then given as follows. Find time dependent functions $u, \vec{x}$ and $\varkappa_\gamma$ such that $u(\cdot,t)\in S_D, \vec{x}(\cdot,t)\in\underline{V}, \varkappa_\gamma(\cdot,t)\in W$ and

$$\vartheta\,(u_t,\phi) + (\mathcal{K}\nabla u,\nabla\phi) - (f,\phi) = -\int_{\Gamma(t)}\left[\mathcal{K}\frac{\partial u}{\partial\vec{\nu}}\right]_{\Gamma(t)}\phi\;ds = \lambda\int_{\Gamma(t)}\vec{x}_t\cdot\vec{\nu}\,\phi\;ds, \quad \forall\,\phi\in S_0, \tag{2.8a}$$

$$\rho\int_{\Gamma(t)}\frac{\vec{x}_t\cdot\vec{\nu}\,\chi}{\beta(\vec{\nu})}\;ds = \int_{\Gamma(t)}[\alpha\varkappa_\gamma - a\,u]\,\chi\;ds \quad \forall\,\chi\in W, \tag{2.8b}$$

$$\int_{\Gamma(t)}\varkappa_\gamma\,\vec{\nu}\cdot\vec{\eta}\;ds + \left\langle\nabla_s^{\widetilde{G}}\vec{x},\nabla_s^{\widetilde{G}}\vec{\eta}\right\rangle_\gamma = 0 \quad \forall\,\vec{\eta}\in\underline{V} \tag{2.8c}$$

hold for almost all times $t\in(0,\overline{T}]$, as well as the initial conditions (2.1e). Here $(\cdot,\cdot)$ denotes the L^2-inner product on Ω. Note that in (2.8a)–(2.8c) for convenience we have adopted a slight abuse of notation. Here and throughout this paper we will identify functions defined on the reference manifold Υ with functions defined on $\Gamma(t)$. In particular, we identify $v\in W$ with $v\circ\vec{x}^{-1}$ on $\Gamma(t)$, where we recall that $\Gamma(t)=\vec{x}(\Upsilon,t)$, and we denote both function simply as v. For example, $\vec{x}\equiv\vec{\mathrm{id}}$ is also the identity function on $\Gamma(t)$. In addition, we have introduced the shorthand notation $\langle\nabla_s^{\widetilde{G}}\cdot,\nabla_s^{\widetilde{G}}\cdot\rangle_\gamma$ for the inner product defined in [9]. In particular, we define the symmetric positive definite matrices $\widetilde{G}_\ell$ with the associated inner products $(\cdot,\cdot)_{\widetilde{G}_\ell}$ on $\mathbb{R}^d$ by

$$\widetilde{G}_\ell := [\det G_\ell]^{\frac{1}{2}}[G_\ell]^{-1} \quad \text{and} \quad (\vec{v},\vec{w})_{\widetilde{G}_\ell} = \vec{v}\cdot\widetilde{G}_\ell\vec{w} \quad \forall\;\vec{v},\vec{w}\in\mathbb{R}^d, \quad \ell = 1\to L.$$

Then we have that:

$$\left\langle\nabla_s^{\widetilde{G}}\vec{\chi},\nabla_s^{\widetilde{G}}\vec{\eta}\right\rangle_\gamma := \sum_{\ell=1}^{L}\int_{\Gamma(t)}\left[\frac{\gamma_\ell(\vec{\nu})}{\gamma(\vec{\nu})}\right]^{r-1}\left(\nabla_s^{\widetilde{G}_\ell}\vec{\chi},\nabla_s^{\widetilde{G}_\ell}\vec{\eta}\right)_{\widetilde{G}_\ell}\gamma_\ell(\vec{\nu})\;ds, \tag{2.9}$$

where

$$\left(\nabla_s^{\widetilde{G}_\ell}\vec{\eta},\nabla_s^{\widetilde{G}_\ell}\vec{\chi}\right)_{\widetilde{G}_\ell} := \sum_{j=1}^{d-1}\left(\partial_{\vec{t}_j^{(\ell)}}\vec{\eta},\partial_{\vec{t}_j^{(\ell)}}\vec{\chi}\right)_{\widetilde{G}_\ell}$$

with $\{\vec{t}_1^{(\ell)},\ldots,\vec{t}_{d-1}^{(\ell)}\}$ being an orthonormal basis with respect to the $\widetilde{G}_\ell$ inner product for the tangent space of $\Gamma(t)$; see [9] for further details. We remark that (2.9) for an isotropic surface energy (2.3) collapses to:

$$\left\langle\nabla_s^{\widetilde{G}}\vec{\chi},\nabla_s^{\widetilde{G}}\vec{\eta}\right\rangle_\gamma = \langle\nabla_s\vec{\chi},\nabla_s\vec{\eta}\rangle := \int_{\Gamma(t)}\nabla_s\vec{\chi}\cdot\nabla_s\vec{\eta}\;ds. \tag{2.10}$$

Moreover, we observe that (2.8b), (2.8c) with $a=0$ collapses to the weak formulation for anisotropic mean curvature flow introduced in [9].

Assuming for simplicity that u_D is constant, we can establish the following a priori bound. Choosing $\phi = u-u_D$ in (2.8a), $\chi=\frac{\lambda}{a}\vec{x}_t\cdot\vec{\nu}$ in (2.8b) and $\vec{\eta}=\frac{\alpha\lambda}{a}\vec{x}_t$ in (2.8c) we obtain, on using the identities:

$$\frac{d}{dt}\,vol(\Omega_s(t)) = \int_{\Gamma(t)}\vec{x}_t\cdot\vec{\nu}\;ds = \int_{\Gamma(t)}\mathcal{V}\;ds, \tag{2.11}$$

see e.g. [23], and

$$\frac{d}{dt}\,|\Gamma(t)|_\gamma = \frac{d}{dt}\int_{\Gamma(t)}\gamma(\vec{\nu})\;ds = \left\langle\nabla_s^{\widetilde{G}}\vec{x},\nabla_s^{\widetilde{G}}\vec{x}_t\right\rangle_\gamma, \tag{2.12}$$

see [9], that:

$$\frac{d}{dt}\left(\frac{\vartheta}{2}\,|u-u_D|_\Omega^2 + \frac{\alpha\lambda}{a}\,|\Gamma(t)|_\gamma + \lambda\,u_D\,vol(\Omega_s(t))\right) + (\mathcal{K}\nabla u,\nabla u) + \frac{\lambda\rho}{a}\int_{\Gamma(t)}\frac{\mathcal{V}^2}{\beta(\vec{\nu})}\;ds = (f,u-u_D), \tag{2.13}$$

where $|\cdot|_\Omega$ denotes the L^2-norm on Ω. Of course, in the case of no-flux Neumann boundary conditions with $\partial_N\Omega=\partial\Omega$, we obtain (2.13) with $u_D=0$.

In addition, in the case of no-flux Neumann boundary conditions with $\partial_N\Omega=\partial\Omega$, and $f\equiv 0$, we have the conservation law:

$$\frac{d}{dt}[\vartheta(u,1)-\lambda\, vol(\Omega_s(t))]=\vartheta(u_t,1)-\lambda\int_{\Gamma(t)}\vec{x}_t\cdot\vec{\nu}\,ds=0. \tag{2.14}$$

These identities follow by integration of (2.1a) using integration by parts, (2.1b), (2.11) and the zero Neumann boundary conditions.

All of the considerations in this section remain valid for the case $\vartheta=\rho=0$. In particular, (2.1a)–(2.1e) with $\vartheta=\rho=0$ is the strong formulation of the Mullins–Sekerka problem, while (2.8a)–(2.8c) with $\vartheta=\rho=0$ is the corresponding weak formulation.

3. Finite element approximation

Let $0=t_0<t_1<\cdots<t_{M-1}<t_M=\overline{T}$ be a partitioning of $[0,\overline{T}]$ into possibly variable time steps $\tau_m:=t_{m+1}-t_m$, $m=0\to M-1$. We set $\tau:=\max_{m=0\to M-1}\tau_m$. First we introduce standard finite element spaces of piecewise linear functions on Ω.

Let Ω be a polyhedral domain. For $m\geqslant 0$, let $\mathcal{T}^m$ be a regular partitioning of Ω into disjoint open simplices, so that $\overline{\Omega}=\cup_{o^m\in\mathcal{T}^m}\overline{o^m}$. Let J^m_Ω be the number of elements in $\mathcal{T}^m$, so that $\mathcal{T}^m=\{o^m_l: l=1\to J^m_\Omega\}$. Associated with $\mathcal{T}^m$ is the finite element space:

$$S^m:=\{\chi\in C(\overline{\Omega}):\chi|_{o^m}\quad\text{is linear }\forall\, o^m\in\mathcal{T}^m\}\subset H^1(\Omega). \tag{3.1}$$

Let K^m_Ω be the number of nodes of $\mathcal{T}^m$ and let $\{\vec{p}^m_j\}_{j=1}^{K^m_\Omega}$ be the coordinates of these nodes. Let $\{\phi^m_j\}_{j=1}^{K^m_\Omega}$ be the standard basis functions for S^m. We introduce $I^m: C(\overline{\Omega})\to S^m$, the interpolation operator, such that $(I^m\eta)(\vec{p}^m_k)=\eta(\vec{p}^m_k)$ for $k=1\to K^m_\Omega$. A discrete semi-inner product on $C(\overline{\Omega})$ is then defined by

$$(\eta_1,\eta_2)^h_m:=(I^m[\eta_1\,\eta_2],1),$$

with the induced semi-norm given by $|\eta|_{\Omega,m}:=[(\eta,\eta)^h_m]^{\frac{1}{2}}$ for $\eta\in C(\overline{\Omega})$.

The test and trial spaces for our finite element approximation of the bulk Eq. (2.8a) are then defined by

$$S^m_0:=\{\chi\in S^m:\chi=0\quad\text{on }\partial_D\Omega\}\quad\text{and}\quad S^m_D:=\{\chi\in S^m:\chi=I^m u_D\quad\text{on }\partial_D\Omega\}, \tag{3.2}$$

where in the definition of S^m_D we allow for $u_D\in H^{\frac{1}{2}}(\partial\Omega)\cap C(\partial\Omega)$.

The parametric finite element spaces in order to approximate $\vec{x}$ and $\varkappa_\gamma$ in (2.8a)–(2.8c), are defined as follows. Similarly to [8], we introduce the following discrete spaces, based on the seminal paper [25]. Let $\Gamma^m\subset\mathbb{R}^d$ be a $(d-1)$-dimensional *polyhedral surface*, i.e. a union of non-degenerate $(d-1)$-simplices with no hanging vertices (see [23, p. 164] for $d=3$), approximating the closed surface $\Gamma(t_m)$, $m=0\to M$. In particular, let $\Gamma^m=\bigcup_{j=1}^{J^m_\Gamma}\overline{\sigma^m_j}$, where $\{\sigma^m_j\}_{j=1}^{J^m_\Gamma}$ is a family of mutually disjoint open $(d-1)$-simplices with vertices $\{\vec{q}^m_k\}_{k=1}^{K^m_\Gamma}$. Then for $m=0\to M-1$, let:

$$\underline{V}(\Gamma^m):=\{\vec{\chi}\in C(\Gamma^m,\mathbb{R}^d):\vec{\chi}|_{\sigma^m_j}\quad\text{is linear}\quad\forall\, j=1\to J^m_\Gamma\}=:[W(\Gamma^m)]^d\subset H^1(\Gamma^m,\mathbb{R}^d),$$

where $W(\Gamma^m)\subset H^1(\Gamma^m,\mathbb{R})$ is the space of scalar continuous piecewise linear functions on Γ^m, with $\{\chi^m_k\}_{k=1}^{K^m_\Gamma}$ denoting the standard basis of $W(\Gamma^m)$. For later purposes, we also introduce $\pi^m: C(\Gamma^m,\mathbb{R})\to W(\Gamma^m)$, the standard interpolation operator at the nodes $\{\vec{q}^m_k\}_{k=1}^{K^m_\Gamma}$, and similarly $\vec{\pi}^m: C(\Gamma^m,\mathbb{R}^d)\to\underline{V}(\Gamma^m)$. Throughout this paper, we will parameterize the new closed surface Γ^{m+1} over Γ^m, with the help of a parameterization $\vec{X}^{m+1}\in\underline{V}(\Gamma^m)$, i.e. $\Gamma^{m+1}=\vec{X}^{m+1}(\Gamma^m)$. Moreover, for $m\geqslant 0$, we will often identify $\vec{X}^m$ with $\vec{\mathrm{id}}\in\underline{V}(\Gamma^m)$, the identity function on Γ^m.

For scalar and vector functions $v,w\in L^2(\Gamma^m,\mathbb{R}^{(d)})$ we introduce the L^2 inner product $\langle\cdot,\cdot\rangle_m$ over the current polyhedral surface Γ^m as follows:

$$\langle v,w\rangle_m:=\int_{\Gamma^m}v\cdot w\,ds.$$

Here and throughout this paper, $\cdot^{(*)}$ denotes an expression with or without the superscript $*$, and similarly for subscripts. If v,w are piecewise continuous, with possible jumps across the edges of $\{\sigma^m_j\}_{j=1}^{J^m_\Gamma}$, we introduce the mass lumped inner product $\langle\cdot,\cdot\rangle^h_m$ as

$$\langle v,w\rangle^h_m:=\frac{1}{d}\sum_{j=1}^{J^m_\Gamma}|\sigma^m_j|\sum_{k=1}^{d}(v\cdot w)\Big((\vec{q}^m_{j_k})^-\Big), \tag{3.3}$$

where $\{\vec{q}^m_{j_k}\}_{k=1}^d$ are the vertices of σ^m_j, and where we define $v((\vec{q}^m_{j_k})^-):=\lim_{\sigma^m_j\ni\vec{p}\to\vec{q}^m_{j_k}}v(\vec{p})$. Here $|\sigma^m_j|=\frac{1}{(d-1)!}|(\vec{q}^m_{j_2}-\vec{q}^m_{j_1})\wedge\cdots\wedge(\vec{q}^m_{j_d}-\vec{q}^m_{j_1})|$ is the measure of σ^m_j, where $\wedge$ is the standard wedge product on $\mathbb{R}^d$.

In addition, we introduce the unit normal $\vec{\nu}^m$ to Γ^m; that is:

$$\vec{\nu}^m_j:=\vec{\nu}^m|_{\sigma^m_j}:=\frac{\left(\vec{q}^m_{j_2}-\vec{q}^m_{j_1}\right)\wedge\cdots\wedge\left(\vec{q}^m_{j_d}-\vec{q}^m_{j_1}\right)}{\left|\left(\vec{q}^m_{j_2}-\vec{q}^m_{j_1}\right)\wedge\cdots\wedge\left(\vec{q}^m_{j_d}-\vec{q}^m_{j_1}\right)\right|},$$

where we have assumed that the vertices $\{\vec{q}^{\,m}_{j_k}\}_{k=1}^{d}$ of σ^m_j are ordered such that $\vec{\nu}^m : \Gamma^m \to \mathbb{R}^d$ induces an orientation on Γ^m. Finally, we set $|\cdot|^2_{m(,h)} := \langle \cdot,\cdot \rangle^{(h)}_m$.

Before we can introduce our approximation to (2.8a)–(2.8c), we have to introduce the notion of a vertex normal on Γ^m. We will combine this definition with a natural assumption that is needed in order to show existence and uniqueness, where applicable, for the introduced finite element approximation.

($\mathcal{A}$) We assume for $m = 0 \to M-1$ that $|\sigma^m_j| > 0$ for all $j = 1 \to J^m_\Gamma$, and that $\Gamma^m \subset \overline{\Omega}$. For $k = 1 \to K^m_\Gamma$, let $\Xi^m_k := \{\sigma^m_j : \vec{q}^{\,m}_k \in \overline{\sigma^m_j}\}$ and set:

$$\Lambda^m_k := \cup_{\sigma^m_j \in \Xi^m_k} \overline{\sigma^m_j} \quad \text{and} \quad \vec{\omega}^m_k := \frac{1}{|\Lambda^m_k|} \sum_{\sigma^m_j \in \Xi^m_k} |\sigma^m_j|\ \vec{\nu}^m_j.$$

Then we further assume that $\vec{\omega}^m_k \neq \vec{0},\ k = 1 \to K^m_\Gamma$, and that $\dim \operatorname{span}\{\vec{\omega}^m_k\}_{k=1}^{K^m_\Gamma} = d, m = 0 \to M-1$.

Given the above definitions, we also introduce the piecewise linear vertex normal function:

$$\vec{\omega}^m := \sum_{k=1}^{K^m_\Gamma} \chi^m_k\, \vec{\omega}^m_k \in \underline{V}(\Gamma^m),$$

and remark that thus:

$$\langle \vec{v}, w\,\vec{\nu}^m \rangle^h_m = \langle \vec{v}, w\,\vec{\omega}^m \rangle^h_m \quad \forall\, \vec{v} \in \underline{V}(\Gamma^m),\ w \in W(\Gamma^m). \tag{3.4}$$

Remark 3.1. We note that one can interpret $\vec{\omega}^m_k$ as a weighted normal defined at the node $\vec{q}^{\,m}_k$ of Γ^m, where in general $|\vec{\omega}^m_k| < 1$. In addition, we note that ($\mathcal{A}$) is only violated in very rare occasions. For example, it always holds for surfaces without self intersections. For more details in the case $d = 2$, we refer to [6].

We consider the following fully practical finite element approximation of (2.8a)–(2.8c). Let Γ^0 and, if $\vartheta > 0, U^0 \in S^0_D$ be given. For $m = 0 \to M-1$, find $U^{m+1} \in S^m_D$, $\vec{X}^{m+1} \in \underline{V}(\Gamma^m)$ and $\kappa^{m+1}_\gamma \in W(\Gamma^m)$ such that:

$$\vartheta \left(\frac{U^{m+1} - U^m}{\tau_m}, \varphi \right)^h_m + \left(\mathcal{K} \nabla U^{m+1}, \nabla \varphi \right) - \lambda \left\langle \pi^m \left[\frac{\vec{X}^{m+1} - \vec{X}^m}{\tau_m} \cdot \vec{\omega}^m \right], \varphi \right\rangle^{\diamondsuit}_m = \left(f^{m+1}, \varphi \right)^h_m \quad \forall\ \varphi \in S^m_0, \tag{3.5a}$$

$$\rho \left\langle [\beta(\vec{\nu}^m)]^{-1} \frac{\vec{X}^{m+1} - \vec{X}^m}{\tau_m}, \chi\, \vec{\omega}^m \right\rangle^h_m - \alpha \left\langle \kappa^{m+1}_\gamma, \chi \right\rangle^h_m + a \left\langle U^{m+1}, \chi \right\rangle^{\diamondsuit}_m = 0 \quad \forall\ \chi \in W(\Gamma^m), \tag{3.5b}$$

$$\left\langle \kappa^{m+1}_\gamma\, \vec{\omega}^m, \vec{\eta} \right\rangle^h_m + \left\langle \nabla^{\widetilde{G}}_s \vec{X}^{m+1}, \nabla^{\widetilde{G}}_s \vec{\eta} \right\rangle_{\gamma,m} = 0 \quad \forall\ \vec{\eta} \in \underline{V}(\Gamma^m), \tag{3.5c}$$

and set $\Gamma^{m+1} = \vec{X}^{m+1}(\Gamma^m)$. In the above, we have $f^{m+1}(\cdot) := f(\cdot, t_{m+1})$ and either:

$$\text{(i)}\ \langle \cdot,\cdot \rangle^{\diamondsuit}_m = \langle \cdot,\cdot \rangle^h_m, \quad \text{or} \quad \text{(ii)}\ \langle \cdot,\cdot \rangle^{\diamondsuit}_m = \langle \cdot,\cdot \rangle^{\star}_m, \quad \text{or} \quad \text{(iii)}\ \langle \cdot,\cdot \rangle^{\diamondsuit}_m = \langle \cdot,\cdot \rangle_m. \tag{3.6}$$

Here in (ii) we consider a discrete inner product on Γ^m that is exact for functions that are piecewise linear on intersections $\sigma^m_j \cap o^m_l$ between Γ^m and the bulk mesh $\mathcal{T}^m$; see Section 4 for details. In addition, for $\vartheta > 0$, the initial value $U^0 \in S^0_D$ is given by $U^0 = I^0[u_0]$, where $u_0 \in C(\overline{\Omega})$ is the given initial data from (2.1e).

We note that the quadrature employed in (3.6)(i), recall (3.3), is exact for functions that are piecewise linear on Γ^m. Finally, for the choice (iii) we need to employ a quadrature that is exact for functions that are piecewise quadratic on intersections $\sigma^m_j \cap o^m_l$ between Γ^m and the bulk mesh; see once again Section 4 for details.

Moreover, $\langle \nabla^{\widetilde{G}}_s \cdot, \nabla^{\widetilde{G}}_s \cdot \rangle_{\gamma,m}$ in (3.5c) is the discrete inner product defined by

$$\left\langle \nabla^{\widetilde{G}}_s \vec{\chi}, \nabla^{\widetilde{G}}_s \vec{\eta} \right\rangle_{\gamma,m} := \sum_{\ell=1}^{L} \int_{\Gamma^m} \left[\frac{\gamma_\ell(\vec{\nu}^{m+1})}{\gamma(\vec{\nu}^{m+1})} \right]^{r-1} \left(\nabla^{\widetilde{G}_\ell}_s \vec{\chi}, \nabla^{\widetilde{G}_\ell}_s \vec{\eta} \right)_{\widetilde{G}_\ell} \gamma_\ell(\vec{\nu}^m)\ ds. \tag{3.7}$$

Note that (3.7) is a natural discrete analogue of (2.9), see [9] for details. The particular choice of normals from the old surface, Γ^m, and the new surface, Γ^{m+1}, ensures that for the solutions to (3.5a)–(3.5c) the weighted surface area $|\Gamma^m|_\gamma$ satisfies a discrete energy law, which mimics the continuous equivalent. In particular, this will lead to unconditionally stable approximations in certain situations; see Theorem 3.1, below. Note that the particular choice of surface normals in (3.7) leads in general to a nonlinear system for $(U^{m+1}, \vec{X}^{m+1}, \kappa^{m+1})$. However, the simpler case $r = 1$ leads to a linear system.

Remark 3.2. Observe that (3.5b), (3.5c) with $a = 0$ and $\beta \equiv 1$, on noting (3.4), collapses to the parametric finite element approximation of anisotropic mean curvature flow introduced in [9].

The following theorem proves existence and uniqueness for a solution to (3.5a)–(3.5c) in the linear case $r = 1$, and establishes a discrete energy bound for general $r \in [1,\infty)$. The lack of an existence proof for $r > 1$ is explained in detail for a related situation in [9, Remark 3.3]. But we note that in practice we had no difficulties in finding solutions to the nonlinear system (3.5a)–(3.5c), and the employed iterative solvers always converged; see Section 4.2 below.

Theorem 3.1. *Let the assumption ($\mathcal{A}$) hold. Then, if $r = 1$, there exists a unique solution $(U^{m+1}, \vec{X}^{m+1}, \kappa_\gamma^{m+1}) \in S_D^m \times \underline{V}(\Gamma^m) \times W(\Gamma^m)$ to (3.5a)–(3.5c). Let $u_D \in \mathbb{R}$, with $u_D = 0$ in the case (2.7)(ii), and define:*

$$\mathcal{E}^m(U^m, \vec{X}^m) := \frac{\vartheta}{2} |U^m - u_D|^2_{\Omega,m} + \frac{\alpha\lambda}{a} |\Gamma^m|_\gamma. \tag{3.8}$$

Then, for $r \in [1,\infty)$, a solution to (3.5a)–(3.5c) satisfies:

$$\begin{aligned} &\mathcal{E}^m\left(U^{m+1}, \vec{X}^{m+1}\right) + \lambda u_D \left\langle \vec{X}^{m+1} - \vec{X}^m, \vec{\omega}^m \right\rangle^h_m + \frac{\vartheta}{2} \left| U^{m+1} - U^m \right|^2_{\Omega,m} + \tau_m \left(\mathcal{K} \nabla U^{m+1}, \nabla U^{m+1} \right) \\ &\quad + \tau_m \frac{\lambda\rho}{a} \left| [\beta(\vec{\nu}^m)]^{-\frac{1}{2}} \frac{\vec{X}^{m+1} - \vec{X}^m}{\tau_m} . \vec{\omega}^m \right|^2_{m,h} \\ &\quad \leqslant \mathcal{E}^m\left(U^m, \vec{X}^m\right) + \tau_m \left(f^{m+1}, U^{m+1} - u_D \right)^h_m. \end{aligned} \tag{3.9}$$

Proof. As the system (3.5a)–(3.5c) is linear for $r = 1$, existence follows from uniqueness. In order to establish the latter, we consider the system: Find $(U, \vec{X}, \kappa_\gamma) \in S_0^m \times \underline{V}(\Gamma^m) \times W(\Gamma^m)$ such that:

$$\vartheta (U, \varphi)^h_m + \tau_m (\mathcal{K} \nabla U, \nabla \varphi) - \lambda \left\langle \pi^m \left[\vec{X} \cdot \vec{\omega}^m \right], \varphi \right\rangle^\diamond_m = 0 \quad \forall \varphi \in S_0^m, \tag{3.10a}$$

$$\frac{\rho}{\tau_m} \left\langle [\beta(\vec{\nu}^m)]^{-1} \vec{X}, \chi \vec{\omega}^m \right\rangle^h_m - \alpha \langle \kappa_\gamma, \chi \rangle^h_m + a \langle U, \chi \rangle^\diamond_m = 0 \quad \forall \chi \in W(\Gamma^m), \tag{3.10b}$$

$$\langle \kappa_\gamma \vec{\omega}^m, \vec{\eta} \rangle^h_m + \left\langle \nabla^{\widetilde{G}}_s \vec{X}, \nabla^{\widetilde{G}}_s \vec{\eta} \right\rangle_{\gamma,m} = 0 \quad \forall \vec{\eta} \in \underline{V}(\Gamma^m). \tag{3.10c}$$

Choosing $\varphi = U$ in (3.10a), $\chi = \frac{\lambda}{a} \pi^m [\vec{X} . \vec{\omega}^m]$ in (3.10b) and $\vec{\eta} = \frac{\alpha\lambda}{a} \vec{X}$ in (3.10c) yields, on noting (3.4), that:

$$\vartheta (U, U)^h_m + \tau_m (\mathcal{K} \nabla U, \nabla U) + \frac{\lambda\rho}{\tau_m a} \left| [\beta(\vec{\nu}^m)]^{-\frac{1}{2}} \vec{X} \cdot \vec{\omega}^m \right|^2_{m,h} + \frac{\alpha\lambda}{a} \left\langle \nabla^{\widetilde{G}}_s \vec{X}, \nabla^{\widetilde{G}}_s \vec{X} \right\rangle_{\gamma,m} = 0. \tag{3.11}$$

It immediately follows from (3.11) that $U \equiv U_c \in \mathbb{R}$, with $U_c = 0$ if $\vartheta > 0$ or $S_0^m \neq S^m$. In addition, on recalling that $\alpha, \lambda > 0$, it holds that $\vec{X} \equiv \vec{X}_c \in \mathbb{R}^d$. Together with (3.10a) and the assumption ($\mathcal{A}$) this immediately yields that $\vec{X} \equiv \vec{0}$, while (3.10c) with $\vec{\eta} = \vec{\pi}^m [\kappa_\gamma \vec{\omega}^m]$ implies that $\kappa_\gamma \equiv 0$. Then it follows from (3.10b) that $U \equiv 0$. Hence there exists a unique solution $(U^{m+1}, \vec{X}^{m+1}, \kappa_\gamma^{m+1}) \in S_D^m \times \underline{V}(\Gamma^m) \times W(\Gamma^m)$.

It remains to establish the bound (3.9). Choosing $\varphi = U^{m+1} - u_D$ in (3.5a), $\chi = \frac{\lambda}{a} \pi^m [(\vec{X}^{m+1} - \vec{X}^m) \cdot \vec{\omega}^m]$ in (3.5b) and $\vec{\eta} = \frac{\alpha\lambda}{a} (\vec{X}^{m+1} - \vec{X}^m)$ in (3.5c) yields that:

$$\begin{aligned} &\vartheta \left(U^{m+1} - U^m, U^{m+1} - u_D \right)^h_m + \tau_m \left(\mathcal{K} \nabla U^{m+1}, \nabla U^{m+1} \right) + \frac{\alpha\lambda}{a} \left\langle \nabla^{\widetilde{G}}_s \vec{X}^{m+1}, \nabla^{\widetilde{G}}_s \left(\vec{X}^{m+1} - \vec{X}^m \right) \right\rangle_{\gamma,m} \\ &\quad + \tau_m \frac{\lambda\rho}{a} \left| [\beta(\vec{\nu}^m)]^{-\frac{1}{2}} \frac{\vec{X}^{m+1} - \vec{X}^m}{\tau_m} \cdot \vec{\omega}^m \right|^2_{m,h} = -\lambda u_D \left\langle \vec{X}^{m+1} - \vec{X}^m, \vec{\omega}^m \right\rangle^h_m + \tau_m \left(f^{m+1}, U^{m+1} - u_D \right)^h_m, \end{aligned}$$

and hence (3.9) follows immediately, where we have used the result that:

$$\left\langle \nabla^{\widetilde{G}}_s \vec{X}^{m+1}, \nabla^{\widetilde{G}}_s (\vec{X}^{m+1} - \vec{X}^m) \right\rangle_{\gamma,m} \geqslant |\Gamma^{m+1}|_\gamma - |\Gamma^m|_\gamma,$$

see e.g. [7] and [9] for the proofs for $d = 2$ and $d = 3$, respectively. □

Remark 3.3. We note that (3.9) closely mimics the corresponding continuous energy law (2.13). The reason why it is not an exact discrete analogue of (2.13) is that in general, the difference $\langle \vec{X}^{m+1} - \vec{X}^m, \vec{\omega}^m \rangle^h_m$ does not correspond to the discrete volume change $vol(\Omega_s^{m+1}) - vol(\Omega_s^m)$, and so we do not control the discrete energy:

$$\widetilde{\mathcal{E}}^m(U^m, \vec{X}^m) := \mathcal{E}^m(U^m, \vec{X}^m) + \lambda u_D \, vol(\Omega_s^m), \tag{3.12}$$

where Ω_s^m is the approximation of the solid region at time t_m. However, on recalling (2.11), we observe that the former difference is an approximation of the latter. Hence we are satisfied that (3.9), in a weak sense, is a discrete analogue of (2.13). Of course, in the trivial case that $u_D = 0$, e.g. when (2.7)(ii) holds, (3.12) reduces to (3.8), the discussed difference term vanishes in (3.9), and an unconditional stability result, based on (3.8) can be shown; see Theorem 3.2 below. Moreover, for a semidiscrete version of our scheme (3.5a)–(3.5c), an exact discrete analogue of (2.13) can be shown; see Remark 3.5 below. Finally, we note that the energy (3.12) always decreased monotonically in all of our numerical experiments in Section 6, with the mesh adaptation strategies described there, when $f^m = 0$, $m = 1 \to M$.

Theorem 3.2. *Let (2.7) hold with $u_D = 0$. In addition, assume that either $\vartheta = 0$ or $U^m \in S_D^m$ for $m = 1 \to M-1$. Then it holds that:*

$$\mathcal{E}^m\Big(U^{m+1},\vec{X}^{m+1}\Big) + \sum_{k=0}^{m}\tau_k\left[\Big(\mathcal{K}\nabla U^{k+1},\nabla U^{k+1}\Big) + \frac{\lambda\rho}{a}\left|\big[\beta(\vec{\nu}^k)\big]^{-\frac{1}{2}}\frac{\vec{X}^{k+1}-\vec{X}^k}{\tau_k}\cdot\vec{\omega}^k\right|^2_{k,h}\right]$$
$$\leqslant \mathcal{E}^0\Big(U^0,\vec{X}^0\Big) + \sum_{k=0}^{m}\tau_k\,\Big(f^{k+1},U^{k+1}-u_D\Big)^h_k \tag{3.13}$$

for $m = 0 \to M-1$.

Proof. The result immediately follows from (3.9) on noting that, if $\vartheta > 0$, it follows from $U^m \in S_D^m$ that $\mathcal{E}^m(U^m,\vec{X}^m) = \mathcal{E}^{m-1}(U^m,\vec{X}^m)$ for $m = 1 \to M-1$. □

Remark 3.4. Theorem 3.2 establishes the unconditional stability of our scheme (3.5a)–(3.5c) under certain conditions. Of course, if $u_D \neq 0$, analogous weaker stability results based on (3.9) can be derived. We note that the condition $U^m \in S_D^m$ is trivially satisfied if $S_D^{m-1} \subset S_D^m$, e.g. when mesh refinement routines without coarsening are employed. In the simpler case that $\vartheta = 0$, the stability bounds (3.13) and (3.9) are independent of U^m and so here stability holds for arbitrary choices of bulk meshes $\mathcal{T}^m$.

Remark 3.5. It is worthwhile to consider a continuous-in-time semidiscrete version of our scheme (3.5a)–(3.5c). Let $\mathcal{T}$ be an arbitrarily fixed triangulation of Ω and define the finite element spaces S, S_0 and S_D similarly to (3.1) and (3.2), with the corresponding lumped inner product $(\cdot,\cdot)^h$ on Ω. Then, given $\Gamma^h(0)$ and, if $\vartheta > 0$, $U(0) \in S_D$, for $t \in (0,\overline{T}]$ find $U(t) \in S_D$, $\vec{X}(t) \in \underline{V}(\Gamma^h(t))$ and $\kappa_\gamma(t) \in W(\Gamma^h(t))$ such that:

$$\vartheta(U_t,\varphi)^h + (\mathcal{K}\nabla U,\nabla\varphi) - \lambda\left\langle\pi^h\Big[\vec{X}_t\cdot\vec{\omega}^h\Big],\varphi\right\rangle^{\diamondsuit}_h = (f,\varphi)^h \quad \forall\,\varphi \in S_0, \tag{3.14a}$$

$$\rho\left\langle\big[\beta(\vec{\nu}^h)\big]^{-1}\vec{X}_t,\chi\,\vec{\omega}^h\right\rangle^h_h - \alpha\,\langle\kappa_\gamma,\chi\rangle^h_h + a\,\langle U,\chi\rangle^{\diamondsuit}_h = 0 \quad \forall\,\chi \in W(\Gamma^h(t)), \tag{3.14b}$$

$$\langle\kappa_\gamma\,\vec{\omega}^h,\vec{\eta}\rangle^h_h + \left\langle\nabla_s^{\widetilde{G}}\vec{X},\nabla_s^{\widetilde{G}}\vec{\eta}\right\rangle_{\gamma,h} = 0 \quad \forall\,\vec{\eta} \in \underline{V}(\Gamma^h(t)), \tag{3.14c}$$

where we always integrate over the current surface $\Gamma^h(t)$, with normal $\vec{\nu}^h(t)$, described by the identity function $\vec{X}(t) \in \underline{V}(\Gamma^h(t))$. In addition, $\vec{\omega}^h$ is the Γ^h analogue of $\vec{\omega}^m$ and $\pi^h : C(\Gamma^h,\mathbb{R}) \to W(\Gamma^h(t))$ is the standard interpolation operator on Γ^h. Moreover, $\langle\cdot,\cdot\rangle^{(h)}_h$ is the same as $\langle\cdot,\cdot\rangle^{(h)}_m$ with Γ^m and $\vec{X}^m$ replaced by Γ^h and $\vec{X}$, respectively; and similarly for $\langle\cdot,\cdot\rangle^{\diamondsuit}_h$ and $\langle\,\cdot\,,\cdot\,\rangle_{\gamma,h}$. For the semidiscrete approximation (3.14a)–(3.14c) we can show the following true volume conservation property in the case $f \equiv 0$ for Neumann boundary conditions, i.e. when $S_0 = S$. First observe that (3.4) yields that:

$$\left\langle\pi^h\Big[\vec{X}_t\cdot\vec{\omega}^h\Big],1\right\rangle^{\diamondsuit}_h = \left\langle\vec{X}_t,\vec{\omega}^h\right\rangle^h_h = \left\langle\vec{X}_t,\vec{\nu}^h\right\rangle^h_h = \int_{\Gamma^h(t)}\vec{X}_t\cdot\vec{\nu}^h\,ds. \tag{3.15}$$

Then, choosing $\varphi = 1$ in (3.14a), we obtain, on noting (3.15) and (2.11), that:

$$\vartheta\,(U_t,1) - \lambda\int_{\Gamma^h(t)}\vec{X}_t\cdot\vec{\nu}^h\,ds = \frac{d}{dt}\Big[\vartheta\,(U,1) - \lambda\,vol\Big(\Omega_s^h(t)\Big)\Big] = 0. \tag{3.16}$$

Clearly, (3.16) is the discrete analogue of (2.14). In addition, using the results from [9] it is straightforward to show that:

$$\frac{d}{dt}|\Gamma^h(t)|_\gamma = \sum_{\ell=1}^{L}\int_{\Gamma^h(t)}\left[\frac{\gamma_\ell(\vec{\nu}^h)}{\gamma(\vec{\nu}^h)}\right]^{r-1}(\nabla_s^{\widetilde{G}_\ell}\vec{X},\nabla_s^{\widetilde{G}_\ell}\vec{X}_t)_{\widetilde{G}_\ell}\,\gamma_\ell(\vec{\nu}^h)\,ds = \left\langle\nabla_s^{\widetilde{G}}\vec{X},\nabla_s^{\widetilde{G}}\vec{X}_t\right\rangle_{\gamma,h},$$

recall (2.9). It is then not difficult to derive the following stability bound for the solution $(U,\vec{X},\kappa_\gamma)$ of the semidiscrete scheme (3.14a)–(3.14c):

$$\frac{d}{dt}\left(\frac{\vartheta}{2}|U-u_D|^2_{\Omega,h}+\frac{\alpha\lambda}{a}\left|\Gamma^h(t)\right|_\gamma+\lambda u_D\, vol\left(\Omega_s^h(t)\right)\right)+(\mathcal{K}\nabla U,\nabla U)+\frac{\lambda\rho}{a}\left|\left[\beta(\vec{v}^h)\right]^{-\frac{1}{2}}\vec{X}_t.\vec{\omega}^h\right|^2_{\Gamma^h,h}=(f,U-u_D)^h, \tag{3.17}$$

where $\Omega_s^h(t)$ is the approximation of the solid region at time t. Clearly, (3.17) is the natural discrete analogue of (2.13).

In addition, it is possible to prove that the vertices of $\Gamma^h(t)$ are well distributed. As this follows already from the Eq. (3.14c), we refer to our earlier works [7,9,8] for further details.

Finally, we remark that (3.14a)–(3.14c) in the case $\vartheta=\rho=f=0$, i.e. our semidiscrete scheme for Mullins–Sekerka in the absence of external heat sources, has a natural interpretation as a spatially discrete gradient flow for the surface energy $|\Gamma|_\gamma$. We refer the interested reader to the Appendix A, where we will give further details on viewing Mullins–Sekerka as a gradient flow and, as a consequence, on an alternative way to introduce the approximations (3.14a)–(3.14c) and (3.5a)–(3.5c) for Mullins–Sekerka.

Remark 3.6. From a practical point of view, it seems natural to also consider decoupled variants of our scheme (3.5a)–(3.5c), where the bulk and interface equations can be solved for independently. Here we note that, if $\rho>0$, it is straightforward to show that, given U^{m+1}, there exists a unique solution $(\vec{X}^{m+1},\kappa_\gamma^{m+1})$ to (3.5b), (3.5c) in the case $r=1$, with practical and reliable solution methods available also for $r>1$; see [9] for details. One such scheme would replace U^{m+1} in (3.5b) with U^m. Then, for $\rho>0$, the adapted (3.5b), (3.5c) can be solved first to obtain $(\vec{X}^{m+1},\kappa_\gamma^{m+1})$, followed by the solution of (3.5a) in order to find U^{m+1}. Of course, this approach breaks down when $\rho=0$, as then the new (3.5b), (3.5c) is no longer uniquely solvable. Moreover, in the case $\vartheta=0$ a suitable U^0 needs to be defined.

A second variant would replace the third term in (3.5a), on recalling (2.1b), (2.1c), with:

$$\frac{\lambda}{\rho}\left\langle\beta(\vec{v}^m)\left[aU^{m+1}-\alpha\kappa_\gamma^m\right],\varphi\right\rangle_m^\diamondsuit,$$

where once again we have assumed that $\rho>0$. Then, on defining a suitable κ_γ^0, the adapted (3.5a) can first be solved in order to find U^{m+1}, followed by the solution of (3.5b), (3.5c) to obtain $(\vec{X}^{m+1},\kappa_\gamma^{m+1})$. This second approach is very close to the procedure adopted in [51]. An advantage of the two modifications discussed above is that, thanks to the decoupling of bulk and interface equation, computing the solution $(U^{m+1},\vec{X}^{m+1},\kappa_\gamma^{m+1})$ is much less involved; see Section 4 below for possible solution methods for the original scheme (3.5a)–(3.5c). However, as we also want to consider quasi-static variants of the Stefan problem, including the case $\rho=0$, and as it does not appear possible to prove stability estimates for the new variants in the spirit of Theorem 3.1, we prefer to use (3.5a)–(3.5c).

3.1. Boundary intersections

In our presentation so far we have assumed that Γ has no boundary, i.e. that $\partial\Gamma(t)=\emptyset$ for $t\in[0,\overline{T}]$. But it is not difficult to generalize our model and our finite element approximation to the case, where the interface Γ intersects the external boundary, i.e. $\partial\Gamma(t)\subset\partial\Omega$.

To this end, we use the techniques introduced in [7] (for $d=2$) and [11] (for $d=3$), in order to generalize the approximation (3.5a)–(3.5c) to this situation. For $m\geqslant 0$ assume that $\partial\Gamma^m\subset\partial\Omega$ and define:

$$\underline{V}_\partial(\Gamma^m):=\left\{\vec{\chi}\in\underline{V}(\Gamma^m):\vec{\chi}(\vec{q})\cdot\vec{\nu}_\Omega=0\quad\forall\,\vec{q}\in\partial\Gamma^m\cap\{\vec{q}_k^m\}_{k=1}^{K_\Gamma^m}\right\}, \tag{3.18}$$

where we recall that as Ω is assumed to be polyhedral, the boundary $\partial\Omega$ is locally flat. Then (3.5a)–(3.5c) is adapted to: Find $U^{m+1}\in S_D^m$, $\delta\vec{X}^{m+1}\in\underline{V}_\partial(\Gamma^m)$ and $\kappa_\gamma^{m+1}\in W(\Gamma^m)$, where $\vec{X}^{m+1}=\vec{X}^m+\delta\vec{X}^{m+1}$, such that:

$$\vartheta\left(\frac{U^{m+1}-U^m}{\tau_m},\varphi\right)_m^h+(\mathcal{K}\nabla U^{m+1},\nabla\varphi)-\lambda\left\langle\pi^m\left[\frac{\delta\vec{X}^{m+1}}{\tau_m}.\vec{\omega}^m\right],\varphi\right\rangle_m^\diamondsuit=(f^{m+1},\varphi)_m^h\quad\forall\,\varphi\in S_0^m, \tag{3.19a}$$

$$\rho\left\langle\left[\beta(\vec{v}^m)\right]^{-1}\frac{\delta\vec{X}^{m+1}}{\tau_m},\chi\,\vec{\omega}^m\right\rangle_m^h-\alpha\left\langle\kappa_\gamma^{m+1},\chi\right\rangle_m^h+a\left\langle U^{m+1},\chi\right\rangle_m^\diamondsuit=0\quad\forall\,\chi\in W(\Gamma^m), \tag{3.19b}$$

$$\left\langle\kappa_\gamma^{m+1}\vec{\omega}^m,\vec{\eta}\right\rangle_m^h+\left\langle\nabla_s^{\widetilde{G}}\vec{X}^{m+1},\nabla_s^{\widetilde{G}}\vec{\eta}\right\rangle_{\gamma,m}=0\quad\forall\,\vec{\eta}\in\underline{V}_\partial(\Gamma^m). \tag{3.19c}$$

We note that the above includes a linearization of the constraint $\partial\Gamma(t)\subset\partial\Omega$, which means that for curved external boundaries $\partial\Omega$ in general it does not hold that $\partial\Gamma^{m+1}\subset\partial\Omega$. For a domain Ω with piecewise flat boundary, as assumed in (3.18), on the other hand, it is easy to show that $\partial\Gamma^{m+1}\subset\partial\Omega$, $m=0\to M-1$, if $\partial\Gamma^0\subset\partial\Omega$. We refer to [7] and [11] for more detailed discussions.

4. Solution of the discrete system

4.1. The linear case

Introducing the obvious abuse of notation, the linear system (3.5a)–(3.5c) in the case $r = 1$ can be formulated as: find $(U^{m+1}, \kappa_\gamma^{m+1}, \delta\vec{X}^{m+1})$ such that:

$$\begin{pmatrix} \frac{1}{\tau_m} M_\Omega + A_\Omega & 0 & -\frac{\lambda}{\tau_m} \vec{N}_{\Gamma,\Omega}^T \\ -a M_{\Gamma,\Omega} & \alpha M_\Gamma & -\frac{\rho}{\tau_m} [\vec{N}_\Gamma^{(\beta)}]^T \\ 0 & \vec{N}_\Gamma & \vec{A}_\Gamma \end{pmatrix} \begin{pmatrix} U^{m+1} \\ \kappa_\gamma^{m+1} \\ \delta\vec{X}^{m+1} \end{pmatrix} = \begin{pmatrix} \frac{1}{\tau_m} M_\Omega U^m \\ 0 \\ -\vec{A}_\Gamma \vec{X}^m \end{pmatrix}, \tag{4.1}$$

where $(U^{m+1}, \kappa_\gamma^{m+1}, \delta\vec{X}^{m+1}) \in \mathbb{R}^{K_\Omega^m} \times \mathbb{R}^{K_\Gamma^m} \times (\mathbb{R}^d)^{K_\Gamma^m}$ here denote the coefficients of these finite element functions with respect to the standard bases of $S_D^m, W(\Gamma^m)$ and $\underline{V}(\Gamma^m)$, respectively. The definitions of the matrices in (4.1) directly follow from (3.5a)–(3.5c), but we state them here for completeness, at least for the case $\partial\Omega = \partial_N\Omega$. Let $i, j = 1 \to K_\Omega^m$ and $k, l = 1 \to K_\Gamma^m$. Then:

$$\begin{aligned} &[M_\Omega]_{ij} := \vartheta \left(\phi_j^m, \phi_i^m\right)^h, \quad [A_\Omega]_{ij} := \left(\mathcal{K} \nabla \phi_j^m, \nabla \phi_i^m\right), \\ &[M_{\Gamma,\Omega}]_{li} := \langle \phi_i^m, \chi_l^m \rangle_m^\diamondsuit, \quad \left[\vec{N}_{\Gamma,\Omega}\right]_{li} := \left(\langle \phi_i^m, \pi^m [(\chi_l^m \vec{e}_j).\vec{\omega}^m] \rangle_m^\diamondsuit\right)_{j=1}^d = \langle \phi_i^m, \chi_l^m \rangle_m^\diamondsuit \vec{\omega}_l^m, \\ &[M_\Gamma]_{kl} := \langle \chi_l^m, \chi_k^m \rangle_m^h, \quad \left[\vec{A}_\Gamma\right]_{kl} := \left(\left\langle \nabla_s^{\widetilde{G}} (\chi_l^m \vec{e}_i), \nabla_s^{\widetilde{G}} (\chi_k^m \vec{e}_j) \right\rangle_{\gamma,m}\right)_{i,j=1}^d, \\ &\left[\vec{N}_\Gamma\right]_{kl} := \langle \chi_l^m, \chi_k^m \vec{\omega}^m \rangle_m^h, \quad \left[\vec{N}_\Gamma^{(\beta)}\right]_{kl} := \left\langle [\beta(\vec{v}^m)]^{-1} \chi_l^m, \chi_k^m \vec{\omega}^m \right\rangle_m^h = \left\langle [\beta(\vec{v}^m)]^{-1} \chi_l^m, \chi_k^m \right\rangle_m^h \vec{\omega}_l^m, \end{aligned} \tag{4.2}$$

where $\{\vec{e}_i\}_{i=1}^d$ denotes the standard basis in $\mathbb{R}^d$ and where we have used the convention that the subscripts in the matrix notations refer to the test and trial domains, respectively. A single subscript is used where the two domains are the same. On observing that M_Γ is a diagonal matrix, that $\vec{N}_\Gamma$ and $\vec{N}_\Gamma^{(\beta)}$ are block diagonal matrices and that $\vec{\omega}_l^m = [M_\Gamma]_{ll}^{-1} [\vec{N}_\Gamma]_{ll}$ we note that:

$$\vec{N}_{\Gamma,\Omega} = \vec{N}_\Gamma M_\Gamma^{-1} M_{\Gamma,\Omega} \quad \text{and} \quad \vec{N}_\Gamma M_\Gamma^{-1} \left[\vec{N}_\Gamma^{(\beta)}\right]^T = \vec{N}_\Gamma^{(\beta)} M_\Gamma^{-1} \vec{N}_\Gamma^T, \tag{4.3a}$$

where the last matrix is a symmetric block diagonal matrix with diagonal entries:

$$\left\langle [\beta(\vec{v}^m)]^{-1} \chi_l^m, \chi_l^m \right\rangle_m^h \vec{\omega}_l^m \otimes \vec{\omega}_l^m, \quad l = 1 \to K_\Gamma^m, \tag{4.3b}$$

which obviously are positive semi-definite $d \times d$ matrices.

If $\rho > 0$, a Schur complement approach can be applied to yield the following reduced system. First we eliminate κ_γ^{m+1} from (4.1) to obtain:

$$\begin{pmatrix} B_\Omega & -\frac{\lambda}{\tau_m} \vec{N}_{\Gamma,\Omega}^T \\ \frac{a}{\alpha} \vec{N}_{\Gamma,\Omega} & \vec{\Lambda}_\Gamma \end{pmatrix} \begin{pmatrix} U^{m+1} \\ \delta\vec{X}^{m+1} \end{pmatrix} = \begin{pmatrix} \frac{1}{\tau_m} M_\Omega U^m \\ -\vec{A}_\Gamma \vec{X}^m \end{pmatrix}, \tag{4.4}$$

where we recall (4.3a), and where:

$$B_\Omega := \frac{1}{\tau_m} M_\Omega + A_\Omega \quad \text{and} \quad \vec{\Lambda}_\Gamma := \vec{A}_\Gamma + \frac{\rho}{\alpha \tau_m} \vec{N}_\Gamma M_\Gamma^{-1} \left[\vec{N}_\Gamma^{(\beta)}\right]^T. \tag{4.5}$$

On noting that $\vec{\Lambda}_\Gamma$, for $\rho > 0$, is symmetric positive definite, recall (4.3a), (4.3b), and hence invertible, we observe that (4.1) can be equivalently formulated as

$$\left(B_\Omega + \frac{\lambda}{\tau_m} \frac{a}{\alpha} \vec{N}_{\Gamma,\Omega}^T \vec{\Lambda}_\Gamma^{-1} \vec{N}_{\Gamma,\Omega}\right) U^{m+1} = \frac{1}{\tau_m} M_\Omega U^m - \frac{\lambda}{\tau_m} \vec{N}_{\Gamma,\Omega}^T \vec{\Lambda}_\Gamma^{-1} \vec{A}_\Gamma \vec{X}^m, \tag{4.6a}$$

and

$$\delta\vec{X}^{m+1} = -\vec{\Lambda}_\Gamma^{-1} \left[\frac{a}{\alpha} \vec{N}_{\Gamma,\Omega} U^{m+1} + \vec{A}_\Gamma \vec{X}^m\right], \tag{4.6b}$$

$$\kappa_\gamma^{m+1} = \frac{1}{\alpha} M_\Gamma^{-1} \left[a M_{\Gamma,\Omega} U^{m+1} + \frac{\rho}{\tau_m} [\vec{N}_\Gamma^{(\beta)}]^T \delta\vec{X}^{m+1}\right]. \tag{4.6c}$$

Clearly, the operator on the left-hand side of (4.6a) is symmetric and positive definite. A natural preconditioner for (4.6a) is B_Ω^{-1}, with the obvious caveat when $\vartheta = 0$ and $\partial_N\Omega = \partial\Omega$. In that case, B_Ω is singular, and the inverse B_Ω^{-1} needs to be replaced with the generalized inverse $\mathcal{R}_\Omega$, see (4.8) below. Finally, a further Schur complement approach would eliminate U^{m+1} from (4.4), and then solve in terms of $\delta\vec{X}^{m+1}$ only. I.e.

$$\left(\vec{A}_\Gamma + \frac{\lambda}{\tau_m}\frac{a}{\alpha}\vec{N}_{\Gamma,\Omega}B_\Omega^{-1}\vec{N}_{\Gamma,\Omega}^T\right)\delta\vec{X}^{m+1} = -\vec{A}_\Gamma\vec{X}^m - \frac{1}{\tau_m}\frac{a}{\alpha}\vec{N}_{\Gamma,\Omega}B_\Omega^{-1}M_\Omega U^m, \tag{4.7a}$$

and

$$U^{m+1} = B_\Omega^{-1}\left[\frac{1}{\tau_m}M_\Omega U^m + \frac{\lambda}{\tau_m}\vec{N}_{\Gamma,\Omega}^T\delta\vec{X}^{m+1}\right], \tag{4.7b}$$

together with (4.6c). Similarly to (4.6a), we note that (4.7a) is a symmetric positive definite system. An advantage of (4.7a) is that it can be applied also in the case $\rho = 0$, however, as noted above, the matrix B_Ω is singular when $\vartheta = 0$ and $\partial_N\Omega = \partial\Omega$. As this situation can arise in practice, e.g. for the Mullins–Sekerka problem with Neumann boundary conditions, we now develop a Schur complement solver for this case.

To this end, we now generalize (4.7a) to the case when the matrix B_Ω, recall (4.5) and (4.2), is singular, i.e. when $\vartheta = 0$ and $\partial_N\Omega = \partial\Omega$, making use of ideas in [6]. Then $B_\Omega = A_\Omega$, with the kernel of A_Ω given as $\ker A_\Omega = \mathrm{span}\{\underline{1}\}$, where $\underline{1} = (1,\ldots,1)^T \in \mathbb{R}^{K_\Omega}$. We introduce the inverse $\mathcal{R}_\Omega$ of A_Ω restricted on the set $(\ker A_\Omega)^\perp$, where $\cdot^\perp$ acting on a space denotes its orthogonal complement, i.e.

$$\mathcal{R}_\Omega A_\Omega\, v = A_\Omega\,\mathcal{R}_\Omega\, v = v \quad \forall\ v \in (\ker A_\Omega)^\perp. \tag{4.8}$$

Then, on noting that the first equation in (4.1) implies that $\underline{1}^T\vec{N}_{\Gamma,\Omega}^T\delta\vec{X}^{m+1} = 0$, we obtain:

$$\left(\vec{A}_\Gamma + \frac{\lambda}{\tau_m}\frac{a}{\alpha}\vec{N}_{\Gamma,\Omega}\Pi_\Omega\mathcal{R}_\Omega\Pi_\Omega\vec{N}_{\Gamma,\Omega}^T\right)\delta\vec{X}^{m+1} = -\vec{A}_\Gamma\vec{X}^m - \xi\frac{a}{\alpha}\vec{N}_{\Gamma,\Omega}\underline{1} \tag{4.9a}$$

and

$$U^{m+1} = \frac{\lambda}{\tau_m}\mathcal{R}_\Omega\vec{N}_{\Gamma,\Omega}^T\delta\vec{X}^{m+1} + \xi\,\underline{1} = \frac{\lambda}{\tau_m}\Pi_\Omega\mathcal{R}_\Omega\Pi_\Omega\vec{N}_{\Gamma,\Omega}^T\delta\vec{X}^{m+1} + \xi\,\underline{1}, \tag{4.9b}$$

where $\xi = [\underline{1}^T\underline{1}]^{-1}\underline{1}^TU^{m+1} \in \mathbb{R}$ is unknown, and where $\Pi_\Omega = Id_{K_\Omega} - \frac{\underline{1}\underline{1}^T}{\underline{1}^T\underline{1}}$ is the orthogonal projection onto $(\ker A_\Omega)^\perp$.

Writing (4.9a) as $\vec{\mathcal{D}}\delta\vec{X}^{m+1} = -\vec{A}_\Gamma\vec{X}^m - \xi\vec{w}$, its solution can be found as follows, where we note that the invertibility of $\mathcal{D}$ follows from Theorem 3.1. Let $\delta\vec{X}_g := -\vec{\mathcal{D}}^{-1}\vec{A}_\Gamma\vec{X}^m$ and $\delta\vec{X}_w := \vec{\mathcal{D}}^{-1}\vec{w}$. Then:

$$\xi = \frac{\underline{1}^T\vec{N}_{\Gamma,\Omega}^T\delta\vec{X}_g}{\underline{1}^T\vec{N}_{\Gamma,\Omega}^T\delta\vec{X}_w} \quad\text{and}\quad \delta\vec{X}^{m+1} = \delta\vec{X}_g - \xi\,\delta\vec{X}_w,$$

is the solution to (4.9a). The remaining part of the solution to (4.1) can then be found via (4.9b) and (4.6c).

4.2. The nonlinear case

For a general $r \in (1,\infty)$ a lagged coefficient fixed point type iteration needs to be employed, i.e. the natural extension of the scheme in [9]. At each time step, given $(U^{m+1,0},\vec{X}^{m+1,0}) := (U^m,\vec{X}^m)$, we seek for $i \geqslant 0$ solutions $(U^{m+1,i+\frac12},\kappa_\gamma^{m+1,i+\frac12},\vec{X}^{m+1,i+\frac12}) \in S_D^m \times W(\Gamma^m) \times \underline{V}(\Gamma^m)$ such that for all $\varphi \in S_0^m$, $\chi \in W(\Gamma^m)$ and $\vec{\eta} \in \underline{V}(\Gamma^m)$:

$$\vartheta\left(\frac{U^{m+1,i+\frac12}-U^m}{\tau_m},\varphi\right)_m^h + (\mathcal{K}\nabla U^{m+1,i+\frac12},\nabla\varphi) - \lambda\left\langle\pi^m\left[\frac{\vec{X}^{m+1,i+\frac12}-\vec{X}^m}{\tau_m}.\vec{\omega}^m\right],\varphi\right\rangle_m^\diamondsuit = (f^{m+1},\varphi)_m^h, \tag{4.10a}$$

$$\rho\left\langle[\beta(\vec{\nu}^m)]^{-1}\frac{\vec{X}^{m+1,i+\frac12}-\vec{X}^m}{\tau_m},\chi\vec{\omega}^m\right\rangle_m^h - \alpha\left\langle\kappa_\gamma^{m+1,i+\frac12},\chi\right\rangle_m^h + a\left\langle U^{m+1,i+\frac12},\chi\right\rangle_m^\diamondsuit = 0, \tag{4.10b}$$

$$\left\langle\kappa_\gamma^{m+1,i+\frac12}\vec{\omega}^m,\vec{\eta}\right\rangle_m^h + \left\langle\nabla_s^{\widetilde{G}}\vec{X}^{m+1,i+\frac12},\nabla_s^{\widetilde{G}}\vec{\eta}\right\rangle_{\gamma,m,i} = 0, \tag{4.10c}$$

where, similarly to (3.7):

$$\left\langle\nabla_s^{\widetilde{G}}\vec{\chi},\nabla_s^{\widetilde{G}}\vec{\eta}\right\rangle_{\gamma,m,i} := \sum_{\ell=1}^{L}\int_{\Gamma^m}\left[\frac{\gamma_\ell(\vec{\nu}^{m+1,i})}{\gamma(\vec{\nu}^{m+1,i})}\right]^{r-1}(\nabla_s^{\widetilde{G}_\ell}\vec{\chi},\nabla_s^{\widetilde{G}_\ell}\vec{\eta})_{\widetilde{G}_\ell}\,\gamma_\ell(\vec{\nu}^m)\,ds = 0.$$

On obtaining $\vec{X}^{m+1,i+\frac12}$ from (4.10a)–(4.10c), e.g. by employing the Schur complement approach as in (4.7a), we set:

$$\vec{X}^{m+1,i+1} = (1-\mu_i)\vec{X}^{m+1,i} + \mu_i\vec{X}^{m+1,i+\frac12}, \tag{4.11}$$

where $\mu_i \in [\mu,1]$ is a damping parameter and $\mu \in (0,1)$ is fixed. The iteration (4.10a)–(4.10c), (4.11) is repeated until

$$\|\vec{X}^{m+1,i+1} - \vec{X}^{m+1,i}\|_\infty < \mathrm{tol}, \tag{4.12}$$

where tol = 10^{-7} is a chosen tolerance. Upon convergence, we fix $\mu_i \equiv 1$ and repeat the iteration for (4.10a)–(4.10c), (4.11) until the criterion (4.12) is satisfied again. On convergence we set $(U^{m+1}, \vec{X}^{m+1}, \kappa_\gamma^{m+1}) := (U^{m+1,i+\frac{1}{2}}, \vec{X}^{m+1,i+\frac{1}{2}}, \kappa_\gamma^{m+1,i+\frac{1}{2}}) \equiv (U^{m+1,i+1}, \vec{X}^{m+1,i+1}, \kappa_\gamma^{m+1,i+1})$. In practice, the described iterative procedure always converged, provided μ and initially μ_i were chosen sufficiently small. The same observation had been made in [9] for essentially the iteration (4.10b), (4.10c), (4.11) with $a = 0$.

4.3. Boundary intersections

The approximation (3.19a)–(3.19c) in the linear case $r = 1$ can be formulated as: find $(U^{m+1}, \kappa_\gamma^{m+1}, \delta\vec{X}^{m+1}) \in \mathbb{R}^{K_\Omega^m} \times \mathbb{R}^{K_\Gamma^m} \times \underline{\mathbb{X}}$ such that:

$$\begin{pmatrix} B_\Omega & 0 & -\frac{\lambda}{\tau_m}\vec{N}_{\Gamma,\Omega}^T \\ -aM_{\Gamma,\Omega} & \alpha M_\Gamma & -\frac{\rho}{\tau_m}\left[\vec{N}_\Gamma^{(\beta)}\right]^T \\ 0 & \Pi_\Gamma \vec{N}_\Gamma & \Pi_\Gamma \vec{A}_\Gamma \end{pmatrix} \begin{pmatrix} U^{m+1} \\ \kappa_\gamma^{m+1} \\ \Pi_\Gamma \delta\vec{X}^{m+1} \end{pmatrix} = \begin{pmatrix} \frac{1}{\tau_m} M_\Omega U^m \\ 0 \\ -\Pi_\Gamma \vec{A}_\Gamma \vec{X}^m \end{pmatrix}, \tag{4.13}$$

where $\Pi_\Gamma : (\mathbb{R}^d)^{K_\Gamma^m} \to \mathbb{X} \subset (\mathbb{R}^d)^{K_\Gamma^m}$ is the orthogonal projection onto the Euclidean vector space associated with $\underline{V}_\delta(\Gamma^m)$. We refer to [7] and [11] for further details.

It is not difficult to generalize the Schur complement approaches (4.7a) and (4.9a) to the linear system (4.13). For example, in the former case, we obtain:

$$\Pi_\Gamma \left(\vec{A}_\Gamma + \frac{\lambda}{\tau_m}\frac{a}{\alpha}\vec{N}_{\Gamma,\Omega} B_\Omega^{-1} \vec{N}_{\Gamma,\Omega}^T \right) \Pi_\Gamma \delta\vec{X}^{m+1} = -\Pi_\Gamma \vec{A}_\Gamma \vec{X}^m - \frac{1}{\tau_m}\frac{a}{\alpha}\vec{N}_{\Gamma,\Omega} B_\Omega^{-1} M_\Omega U^m \tag{4.14}$$

and (4.7b), (4.6c), on noting that $\Pi_\Gamma\, \delta\vec{X}^{m+1} = \delta\vec{X}^{m+1}$.

4.4. Direct and iterative solvers

One can solve (4.1) or (4.4) either with a sparse direct solver such as UMFPACK, see [21]; or with an iterative solver for one of the previously introduced Schur complement approaches. For the computations presented in this paper, we always use iterative solvers, and we only compute the values that are needed. In particular, for the Stefan problem one only needs to compute $\vec{X}^{m+1}$ and U^{m+1}, while for the Mullins–Sekerka problem one only needs to compute $\vec{X}^{m+1}$.

If $\rho > 0$, then we compute the discrete solutions with a preconditioned conjugate gradient (pCG) solver for (4.6a). Here the applications of Λ_Γ^{-1} and the preconditioner B_Ω^{-1} are computed exactly, with the help of sparse direct solvers for symmetric positive definite matrices. We employ the sparse LDL^T factorization package LDL ([22]), together with the sparse matrix ordering package AMD ([2]). For large scale three dimensional computations the direct factorization of B_Ω can become inefficient. Then, as an alternative, the action of B_Ω^{-1} may also be computed with the help of a multigrid solver.

In the case $\rho = 0$ we use a pCG solver for (4.7a) and (4.9a), respectively. Here the actions of B_Ω^{-1} and $\mathcal{R}_\Omega$ are once again computed with the help of either LDL/AMD or a multigrid solver. In addition, we employ the inverses of $\mathrm{diag}(\vec{\Lambda}_\Gamma)$ or

$$\vec{L}_\Gamma := \vec{\Lambda}_\Gamma + \frac{a}{\alpha}\frac{\lambda}{\tau_m}\vec{N}_{\Gamma,\Omega}\,\mathrm{diag}(B_\Omega)^{-1}\vec{N}_{\Gamma,\Omega}^T$$

as preconditioners, where the latter is not always sparse and hence not always practical.

The linear system (4.13), is always solved with the help of a pCG solver for (4.14) or, in the case that B_Ω is singular, with the obvious analogue of (4.14). In the former case, the preconditioners Λ_Γ^{-1} when $\rho > 0$, and $[\mathrm{diag}\,(\Lambda_\Gamma)]^{-1}$ when $\rho = 0$ prove efficient, whereas in the latter case we employ $\Pi_\Omega \Lambda_\Gamma^{-1} \Pi_\Omega$ and $\Pi_\Omega[\mathrm{diag}\,(\Lambda_\Gamma)]^{-1}\Pi_\Omega$, respectively.

4.5. Assembly of interface-bulk cross terms

We note that the assembly of the matrices arising from (3.5a)–(3.5c) is mostly standard. For the cross terms between bulk mesh and parametric mesh one needs to compute contributions of the form:

$$\text{(i)}\ \left\langle \phi_i^m, \chi_j^m \right\rangle_m^h = \phi_i^m(\vec{q}_j^m)\left\langle \chi_j^m, \chi_j^m \right\rangle_m^h, \quad \text{(ii)}\ \left\langle \phi_i^m, \chi_j^m \right\rangle_m^{\star}, \quad \text{(iii)}\ \left\langle \phi_i^m, \chi_j^m \right\rangle_m, \tag{4.15}$$

where $\{\phi_i^m\}_{i=1}^{K_\Omega^m}$ and $\{\chi_j^m\}_{j=1}^{K_\Gamma^m}$ are the canonical basis functions of S^m and $W(\Gamma^m)$, respectively. In the following, we state precisely how (4.15) can be computed in practice. Clearly, (4.15)(i) only needs to evaluate the bulk basis function ϕ_i^m at the vertex $\vec{q}_j^m$ of Γ^m; a simple task. For the choices (ii) and (iii), on the other hand, we need to compute the intersections between bulk elements o_l^m and surface mesh elements σ_j^m. For notational convenience, we will drop the subscripts l and j in the remainder of this subsection.

In two space dimensions, i.e. $d = 2$, the intersection of a segment σ^m of the polygonal curve Γ^m and a bulk mesh element $o^m \in \mathcal{T}^m$ is always given by a segment, say $o^m \cap \sigma^m = [\vec{q}_1, \vec{q}_2]$. Then the contribution over $[\vec{q}_1, \vec{q}_2]$ for (4.15)(ii) is

$$\left\langle \phi_i^m, \chi_j^m \right\rangle^{\star}_{[\vec{q}_1,\vec{q}_2]} := \frac{1}{2}|\vec{q}_1 - \vec{q}_2| \sum_{k=1}^{2} \phi_i^m(\vec{q}_k)\chi_j^m(\vec{q}_k). \tag{4.16a}$$

Similarly, the contribution over $[\vec{q}_1, \vec{q}_2]$ for (4.15)(iii) is

$$\left\langle \phi_i^m, \chi_j^m \right\rangle_{[\vec{q}_1,\vec{q}_2]} := \frac{1}{6}|\vec{q}_1 - \vec{q}_2| \sum_{k=0}^{2} \omega_k \phi_i^m(\vec{q}_k)\chi_j^m(\vec{q}_k), \tag{4.16b}$$

where $\vec{q}_0 := \frac{1}{2}\sum_{k=1}^{2}\vec{q}_k$ and $\omega_0 = \frac{2}{3}$, $\omega_1 = \omega_2 = \frac{1}{6}$ from Simpson's rule.

The natural generalizations of (4.16a), (4.16b) to $d = 3$ are given as follows. Here the intersection of a triangular element σ^m of the polyhedral surface Γ^m with a bulk mesh element o^m is a convex l-polygon $\mathcal{P}$, with $3 \leqslant l \leqslant 7$. Some example intersections are given in Fig. 4, with our algorithm to compute $\mathcal{P}$ stated below. Then the contribution over $\mathcal{P} \equiv \mathrm{conv}(\{\vec{q}_i\}_{i=1}^{l})$ for (4.15)(ii) is

$$\langle \phi_i^m, \chi_j^m \rangle^{\star}_{\mathcal{P}} := \sum_{k=0}^{l} \omega_k^{\mathcal{P}} \phi_i^m(\vec{q}_k)\chi_j^m(\vec{q}_k),$$

where $\vec{q}_0 := \frac{1}{l}\sum_{k=1}^{l}\vec{q}_k$ is the centroid of $\mathcal{P}$ and the weights $\omega_k^{\mathcal{P}}$ are easily defined such that $\langle \varphi, 1\rangle_m^h = \langle \varphi, 1\rangle_m$ for all $\varphi \in S^m$, by partitioning $\mathcal{P}$ into triangles having $\vec{q}_0$ as a vertex; see Fig. 5. Similarly, the contribution over $\mathcal{P}$ for (4.15)(iii) is

$$\left\langle \phi_i^m, \chi_j^m \right\rangle_{\mathcal{P}} := \sum_{k=1}^{2l} \omega_k^{\mathcal{P}} \phi_i^m(\vec{p}_k)\chi_j^m(\vec{p}_k),$$

where $\vec{p}_k := \frac{1}{2}[\vec{q}_0 + \vec{q}_k]$ and $\vec{p}_{l+k} := \frac{1}{2}[\vec{q}_k + \vec{q}_{k+1}]$ for $k = 1 \to l$, where $\vec{q}_{l+1} := \vec{q}_1$. The weights $\omega_k^{\mathcal{P}}$ are easily defined such that $\langle \varphi, \chi\rangle_m^h = \langle \varphi, \chi\rangle_m$ for all $\varphi \in S^m$ and all $\chi \in W(\Gamma^m)$, by partitioning $\mathcal{P}$ into triangles having $\vec{q}_0$ as a vertex; see Fig. 5.

We now describe our algorithm for finding the intersection $\mathcal{P} = o^m \cap \sigma^m$ between a bulk element o^m and a parametric element σ^m in $\mathbb{R}^3$.

1. For each vertex of the triangle σ^m, test whether it is inside the tetrahedra o^m. If it is, add it to the list of vertices of $\mathcal{P}$.
2. For each edge of σ^m with at least one vertex not inside o^m, test whether it intersects any of the four faces of o^m. If it does so, add the intersection to the set of vertices of $\mathcal{P}$.
3. For each of the six edges of o^m, test whether it intersects σ^m. If it does, add the intersection to the set of vertices of $\mathcal{P}$.
4. Remove any duplicate vertex in $\mathcal{P}$.

The above algorithm computes $\mathcal{P} = o^m \cap \sigma^m$ for a given pair of elements. In order to find all such pairs with nonempty intersection $\mathcal{P}$, we employ for each parametric element σ^m a hierarchical search in the bulk mesh tree, in order to find all bulk elements o^m that have nonempty intersection with it. Hence the overall complexity of assembling the matrices $M_{\Gamma,\Omega}$

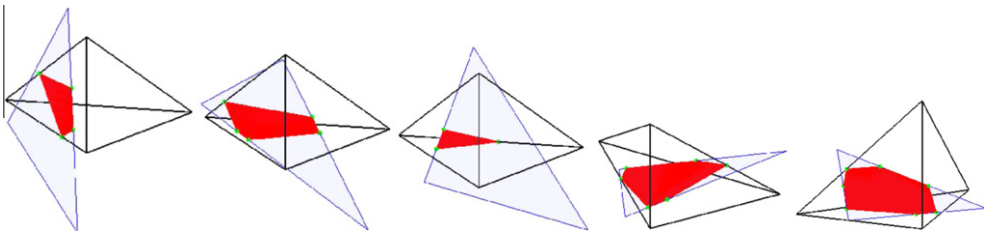

Fig. 4. Intersections of a triangle and a simplex in $\mathbb{R}^3$.

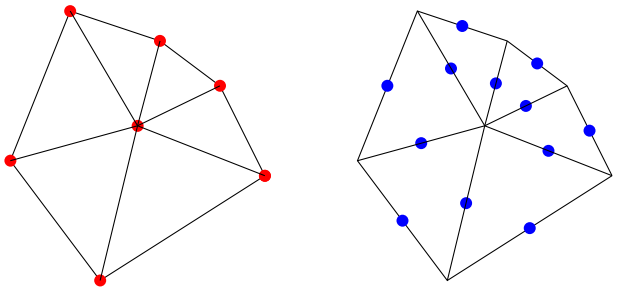

Fig. 5. Sketch of $\mathcal{P}$ with sampling points for (4.15)(ii) (left) and (4.15)(iii) (right).

and $\vec{N}_{\Gamma,\Omega}$ is $\mathcal{O}(J^m_\Gamma \log J^m_\Omega)$. Better complexities have recently been shown for triangle-triangle and tetrahedra-tetrahedra mesh intersections, on utilizing commonly available element neighbouring information; see [30].

5. Mesh adaptation

We implemented our finite element approximation (3.5a)–(3.5c) within the framework of the finite element toolbox ALBERTA, see [53]. In what follows we describe the mesh refinement strategies used for both bulk and interface mesh.

5.1. Bulk mesh adaptation

Given a polyhedral approximation Γ^m, $m \geqslant 0$, of the interface, we employ the following mesh adaptation strategy for the bulk mesh triangulation $\mathcal{T}^m$. The strategy is inspired by a similar refinement algorithm proposed in [12] and [3] for $d = 2$ and $d = 3$, respectively. It results in a fine mesh around Γ^m and a coarse mesh further away from it.

In particular, given two integer parameters $N_f > N_c$, we set $h_f = \frac{2H}{N_f}, h_c = \frac{2H}{N_c}$, where for simplicity we assume that $\Omega = (-H,H)^d$. Then we set:

$$vol_f = \frac{h_f^d}{d!} \quad \text{and} \quad vol_c = \frac{h_c^d}{d!},$$

that is, for $d = 3$, vol_f denotes the volume of a tetrahedron with three right-angled and isosceles faces with side length h_f, while for $d = 2$ it denotes the area of a right-angled and isosceles triangle with side length h_f, and similarly for vol_c.

Now starting with the triangulation $\mathcal{T}^{m-1}$ from the previous time step, where here for convenience we define $\mathcal{T}^{-1}$ to be a uniform partitioning of mesh size h_c, we obtain $\mathcal{T}^m$ as follows. First any element $o^{m-1} \in \mathcal{T}^{m-1}$ satisfying $|o^{m-1}| \geqslant 2\ vol_f$ and $o^{m-1} \cap \Gamma^m \neq \emptyset$ is marked for refinement. In addition, any element satisfying $|o^{m-1}| \geqslant 2\ vol_f$, for which a direct neighbour intersects Γ^m, is also marked for refinement. Similarly, an element that is not marked for refinement is marked for coarsening if it satisfies $|o^{m-1}| \leqslant \frac{1}{2}\ vol_c$ and $o^{m-1} \cap \Gamma^m = \emptyset$. Now all the elements marked for refinement are halved into two smaller elements with the help of a simple bisectioning procedure, see [53] for details. In order to avoid hanging nodes, this will in general lead to refinements of elements that were not originally marked for refinement. Similarly, an element that is marked for coarsening is coarsened only if all of its neighbouring elements are marked for coarsening as well. For more details on the refining and coarsening itself we refer to [53].

This marking and refinement process is repeated until no more elements are required to be refined or coarsened. Thus we obtain the triangulation $\mathcal{T}^m$ on which, together with Γ^m, the new solutions $(U^{m+1}, \vec{X}^{m+1}, \kappa_\gamma^{m+1})$ will be computed. In practice only at the first time step, $m = 0$, more then one of the described refinement cycles are needed.

We note that, as observed in Remark 3.4, the coarsening in the above described mesh adaptation means that for $\vartheta > 0$ the conditions of Theorem 3.2 are in general not satisfied.

5.2. Parametric mesh adaptation

As mentioned before, the Eq. (3.5c) means that the vertices of the parametric approximation Γ^m are in general very well distributed, so that mesh smoothing (redistribution) is not necessary in practice. Similarly, an adaptation of the parametric mesh is in general not necessary. However, in almost all of our presented simulations, the total surface area $|\Gamma^m|$ increases significantly over time. Hence constant-in-time parametric discretization parameters will either mean that the interface is initially "over-resolved", which is computationally inefficient, or that the interface approximation lacks accuracy at later stages. Hence, we consider a very simple adaptive strategy that will lead to an efficient algorithm, as well as accurate resolution of the interface throughout. In addition, this strategy will mean that both the bulk mesh size around the interface, as well as the parametric mesh size on the interface will be of the same order throughout the evolution.

The mesh refinement strategy can be described as follows, where we assume that an arbitrary polyhedral approximation Γ^0 of $\Gamma(0)$ is given. Let:

$$vol_{\max} := \max_{j=1\to J^0_\Gamma} |\sigma^0_j|.$$

Then for an arbitrary $m \geqslant 0$, given Γ^m and the solution $(U^{m+1}, \vec{X}^{m+1}, \kappa_\gamma^{m+1})$ to (3.5a)–(3.5c), we define $\Gamma^{m+1,\star} := \vec{X}^{m+1}(\Gamma^m)$. Clearly, $\Gamma^{m+1,\star} = \bigcup_{j=1}^{J^m_\Gamma} \overline{\sigma^{m+1,\star}_j}$, where $\sigma^{m+1,\star}_j := \vec{X}^{m+1}(\sigma^m_j),\ j = 1 \to J^m_\Gamma$. We will now define a finer triangulation $\bigcup_{j=1}^{J^{m+1}_\Gamma} \overline{\sigma^{m+1}_j}$, with $J^{m+1}_\Gamma \geqslant J^m_\Gamma$, for the same polyhedral surface $\Gamma^{m+1,\star} = \Gamma^{m+1}$. To this end, we mark all elements $\sigma^{m+1,\star}_j$, that have become too large due to the growth of the interface, for refinement. In particular, any element with $|\sigma^{m+1,\star}_j| \geqslant \frac{7}{4}\ vol_{\max}$ is marked for refinement. Then all refined elements are replaced with two smaller ones with the help of a simple bisectioning procedure. Note that this bisection does not change the polyhedral surface $\Gamma^{m+1,\star} = \Gamma^{m+1}$. Moreover, we note that in order to prevent hanging nodes, in general more elements will be refined than have initially been marked for refinement. The cycle of marking and refining is repeated until no more refinements are required. In practice, this was always the case after just one such refinement step.

In conclusion we stress that the given parametric mesh adaptation algorithm means that Theorem 3.2 still holds. Moreover, apart from this simple mesh refinement, no other changes were performed on the parametric mesh in any of our simulations. In particular, no mesh smoothing (redistribution) was required.

6. Numerical results

For the numerical results in this paper, for simplicity, we restrict ourselves to the case of constant heat conductivity $\mathcal{K}$. The case of piecewise constant coefficients is numerically more involved, and this will be addressed in a forthcoming paper. We refer to [4], see also [5], for a possible natural approach in this case.

Throughout this section we use (almost) uniform time steps; in that, $\tau_m = \tau$, $m = 0 \to M-2$, and $\tau_{M-1} = T - t_{m-1} \leqslant \tau$. Moreover, unless otherwise stated, we always employ (3.6)(iii), i.e. we integrate these cross terms exactly.

For later use, we define $h_\Gamma^m := \max_{j=1\to J_\Gamma^m} \mathrm{diam}(\sigma_j^m)$. We also define the errors $\|\vec{X} - \vec{x}\|_{L^\infty} := \max_{m=1\to M} \|\vec{X}^m - \vec{x}(\cdot, t_m)\|_{L^\infty}$, where $\|\vec{X}(t_m) - \vec{x}(\cdot, t_m)\|_{L^\infty} := \max_{k=1\to K_\Gamma^m} \{\min_{\vec{y}\in\Upsilon} |\vec{X}^m(\vec{q}_k^m) - \vec{x}(\vec{y}, t_m)|\}$ and $\|U - I^h u\|_{L^\infty} := \max_{m=1\to M} \|U^m - I^m u(\cdot, t_m)\|_{L^\infty}$.

6.1. Non-dimensionalization

In order to study the parameter dependence of the numerical simulations in a systematic way, a non-dimensionalization of the Stefan problem is necessary. Introducing characteristic scales $\tilde{z}, \tilde{t}, \tilde{u}$ and $\tilde{f}$ for space, time, temperature and heat sources, we non-dimensionalize the variables as follows:

$$\widehat{\vec{z}} = \tilde{z}^{-1}\vec{z}, \quad \widehat{t} = \tilde{t}^{-1}t, \quad \widehat{u} = \tilde{u}^{-1}u, \quad \widehat{f} = \tilde{f}^{-1}f.$$

Let the capillary length d_0 be defined by $d_0 = \frac{\alpha\vartheta T_M}{\lambda^2}$, which is an important length scale for solidification phenomena. Then let:

$$\varrho : \frac{\rho\mathcal{K}T_M}{\lambda^2\tilde{z}} \qquad \text{and} \qquad \varsigma := \frac{d_0}{\tilde{z}} = \frac{\alpha\vartheta T_M}{\lambda^2\tilde{z}}$$

denote a dimensionless kinetic coefficient and a dimensionless capillary coefficient, respectively, where we recall the notation and scaling in (2.2), and where we assume that $\mathcal{K}$ is constant in Ω and that $\vartheta > 0$. Denoting by T_D a typical temperature in the problem, e.g. the temperature at the boundary, we obtain two important scalings for (2.1a)–(2.1e). It will turn out that in both scalings the dimensionless undercooling $\mathcal{S} = \frac{(T_M - T_D)\vartheta}{\lambda}$, as well as the dimensionless capillary coefficient ς, will be important parameters.

Scaling I: $\tilde{t} = \frac{\vartheta\tilde{z}^2}{\mathcal{K}}$, $\tilde{u} = T_M - T_D$, $\tilde{f} = \frac{\mathcal{K}\tilde{u}}{\tilde{z}^2}$.
This scaling leads to (we drop the ^ in the rescaled variables):

$$u_t - \Delta u = f \quad \text{in } \Omega_s(t) \cup \Omega_l(t), \quad \left[\frac{\partial u}{\partial \vec{\nu}}\right]_{\Gamma(t)} = -\mathcal{S}^{-1}\mathcal{V} \quad \text{on } \Gamma(t), \tag{6.1a}$$

$$\frac{\varrho}{\beta(\vec{\nu})}\mathcal{V} = \varsigma\varkappa_\gamma - \mathcal{S}u \quad \text{on } \Gamma(t), \tag{6.1b}$$

$$\frac{\partial u}{\partial \vec{\nu}_\Omega} = 0 \quad \text{on } \partial_N\Omega, \quad u = -1 \quad \text{on } \partial_D\Omega, \quad \Gamma(0) = \Gamma_0, \quad u(\cdot, 0) = u_0 \quad \text{in } \Omega. \tag{6.1c}$$

For a given constant temperature at the boundary, a certain multiple of the Wulff shape is stationary, where the Wulff shape, recall (2.5), is a region with a boundary such that $\varkappa_\gamma = -1$, see [35]. Examining (6.1b) we observe that we have to scale the Wulff shape by $R_c = \frac{\varsigma}{\mathcal{S}}$ in order to obtain a stationary shape. In the isotropic case R_c is called the critical nucleation radius and it turns out that balls with a radius smaller than R_c shrink and larger ones grow. One observes that the critical nucleation radius becomes smaller for large undercoolings and for small surface energy densities.

Scaling II: $\tilde{t} = \frac{\tilde{z}^2\lambda}{\mathcal{K}\tilde{u}}$, $\tilde{u} = T_M - T_D$, $\tilde{f} = \frac{\mathcal{K}\tilde{u}}{\tilde{z}^2}$.
The nondimensional equations are now (we again drop the ^ in the rescaled variables):

$$\mathcal{S}\partial_t u - \Delta u = f \quad \text{in } \Omega_s(t) \cup \Omega_l(t), \quad \left[\frac{\partial u}{\partial \vec{\nu}}\right]_{\Gamma(t)} = -\mathcal{V} \quad \text{on } \Gamma(t), \tag{6.2a}$$

$$\frac{\varrho}{\beta(\vec{\nu})}\mathcal{V} = \frac{\varsigma}{\mathcal{S}}\varkappa_\gamma - u \quad \text{on } \Gamma(t), \quad \text{and} \quad (6.1c). \tag{6.2b}$$

For small undercoolings $\mathcal{S}$, with $\frac{\varsigma}{\mathcal{S}}$ still of order one, and in addition with $\frac{\varrho}{\beta(\vec{\nu})}$ small, we can neglect the terms $\mathcal{S}\partial_t u$ in (6.2a) and $\frac{\varrho}{\beta(\vec{\nu})}\mathcal{V}$ in (6.2b), and then obtain the Mullins–Sekerka problem:

$$-\Delta u = 0 \quad \text{in } \Omega_s(t) \cup \Omega_l(t), \quad \left[\frac{\partial u}{\partial \vec{\nu}}\right]_{\Gamma(t)} = -\mathcal{V} \quad \text{on } \Gamma(t), \tag{6.3a}$$

$$0 = \frac{\varsigma}{\mathcal{S}}\varkappa_\gamma - u \quad \text{on } \Gamma(t), \tag{6.3b}$$

$$\frac{\partial u}{\partial \vec{\nu}_\Omega} = 0 \quad \text{on } \partial_N\Omega, \quad u = -1 \quad \text{on } \partial_D\Omega, \quad \Gamma(0) = \Gamma_0. \tag{6.3c}$$

All our reported numerical experiments will be for the rescaled problems (6.1a)–(6.1c), for the Stefan problem, and (6.3a)–(6.3c), for the Mullins–Sekerka problem. Unless otherwise stated, we will use $\mathcal{S} = 1$, $\beta = \gamma$, $f = 0$ and $\Omega = (-H,H)^d$ with $H = 4$. For computations for the Stefan problem (6.1a)–(6.1c) we will in general take $\varsigma = 10^{-3}$, $\varrho = 10^{-2}$ and (2.7)(i), while for the Mullins–Sekerka problem (6.3a)–(6.3c), we usually set $\varsigma = 1$ and take (2.7)(ii).

The initial interface $\Gamma(0)$ is either a circle/sphere of radius $R_0 \in (0,H)$ around the origin, or a (perturbed) straight horizontal line in $\mathbb{R}^2$, with endpoints attached to $\partial\Omega$. For the Stefan problem (6.1a)–(6.1c), in the former case, we set:

$$u_0(\vec{z}) = \begin{cases} 0 & |\vec{z}| \leqslant R_0, \\ -\frac{1-e^{R_0-|\vec{z}|}}{1-e^{R_0-H}} & R_0 < |\vec{z}| < H, \\ -1 & |\vec{z}| \geqslant H; \end{cases}$$

while for a straight line at height $z_2 = H_0 \in (-H,H)$, we set:

$$u_0(\vec{z}) = \begin{cases} 0 & z_2 \leqslant H_0, \\ -\frac{1-e^{H_0-z_2}}{1-e^{H_0-H}} & H_0 < z_2 < H, \\ -1 & z_2 \geqslant H; \end{cases}$$

unless a true solution u is given.

6.2. Planar Mullins–Sekerka instability

As mentioned in Section 1, the instability of a straight planar interface in the presence of undercooling was first analysed in [46]. Here we numerically investigate this instability for a straight line in $\mathbb{R}^2$. In this context we refer to [57], where the stability of a flat interface for a semidiscrete, quasi-stationary variant of the Stefan problem was studied. For the numerical investigations in this section, we let $\Gamma(0)$ be a straight horizontal line at height $z_2 = -3$ within the domain $\Omega = (-4,4)^2$, i.e. $H = 4$. The liquid phase is undercooled from the upper boundary, so that $\partial_D\Omega = [-4,4] \times \{4\}$, which corresponds to (2.7)(iii). Clearly, for the given setup an exact solution can be computed, which is given by the interface moving unchanged through the domain towards the upper boundary. However, this solution is unstable. In order to investigate this instability, we perturb the initial interface $\Gamma(0)$ slightly with the following perturbation. Let:

$$\zeta(\vec{z}) = \sum_{j=1}^{30} \delta_j \cos\left(\frac{j\pi}{4} z_1\right), \tag{6.4}$$

where $|\delta_j| \leqslant 0.01$ are some randomly chosen values. Then we add this perturbation to the straight interface, i.e. $\Gamma(0)$ is replaced by $\Gamma(0) + \zeta(\Gamma(0))\vec{e}_2$. As (6.4) is clearly an even function with respect to the z_1-coordinate, the evolution will be symmetric with respect to the z_2-axis throughout. If the numerical results also show this symmetry, then this will be a strong indication that all of the observed instabilities, such as fingering and sidebranching, are due to the chosen perturbation (6.4) only, and are unlikely to be caused by numerical noise.

In the following experiments for (6.1a)–(6.1c), for an isotropic surface energy (2.3), we vary ς and keep all the other parameters fixed as previously described. The discretization parameters are $N_f = 4096$, $N_c = 256$, $\tau = 10^{-4}$ and $K_\Gamma^0 = 4097$. See Fig. 6 for the different evolutions for $\varsigma = 5 \times 10^{-3}$, 2×10^{-3} and 10^{-3}, where in all of the computations we observe the expected symmetry. We note that each computation was stopped when the discrete interface no longer remained entirely in $\overline{\Omega}$. Moreover, in Fig. 7 we show the results for the same experiments but now for $\mathcal{S} = \frac{5}{4}$, which has an immediate and noticeable effect on the evolution as $\overline{T}$ is much smaller.

The same experiments, for the anisotropy γ as in the middle of Fig. 2, can be seen in Figs. 8 and 9. We observe that for both sets of experiments, the instability becomes stronger for smaller values of ς, and for larger values of $\mathcal{S}$. In particular, we observe that for ς getting smaller, the fastest growing modes represented in the initial data become more and more oscillatory. Moreover, as expected, the branching in the anisotropic setting in Fig. 8 is clearly aligned with the coordinate axes, while in the isotropic case there is no clear preferred growth direction.

6.3. Convergence experiment for the Stefan problem

We start with a comparison of our algorithm (3.5a)–(3.5c) for a known exact solution to the Stefan problem (6.1a)–(6.1c) in the case of an isotropic surface energy (2.3). Here we use the expanding circle/sphere solution introduced in [51, pp. 303–304], where the radius of the circle/sphere is given by $r(t)$. Assume that $\varsigma = \varrho$ and let:

$$r(t) = (r^2(0) + t)^{\frac{1}{2}}, \quad w(t) = -\frac{\varsigma(d-\frac{1}{2})}{r(t)}, \quad v(s) = -\frac{e^{\frac{1}{4}}}{2}\int_1^s \frac{e^{-\frac{1}{4}z^2}}{z^{d-1}}\,dz.$$

Then it is easy to see that on letting:

$$f(\vec{z},t) = \frac{d}{dt}w(t) = \frac{\varsigma(d-\frac{1}{2})}{2r^3(t)},$$

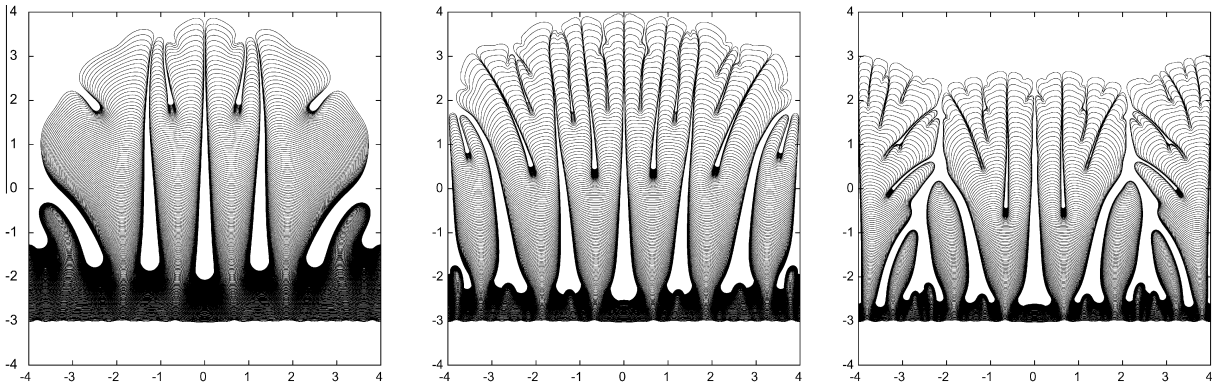

Fig. 6. $\vec{X}(t)$ at times $t = 0, 0.01, \ldots, \overline{T}$ with $\overline{T} = 2.21, 1.63, 1.29$ for $\mathcal{S} = 1$ and $\varsigma = 5 \times 10^{-3}$, 2×10^{-3}, 10^{-3}, respectively.

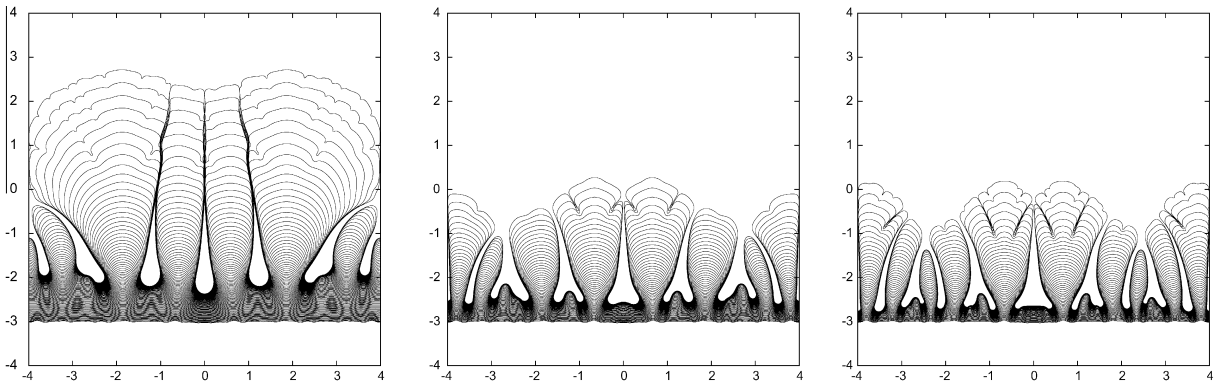

Fig. 7. $\vec{X}(t)$ at times $t = 0, 0.01, \ldots, \overline{T}$ with $\overline{T} = 0.88, 0.59, 0.52$ for $\mathcal{S} = \frac{5}{4}$ and $\varsigma = 5 \times 10^{-3}$, 2×10^{-3}, 10^{-3}, respectively.

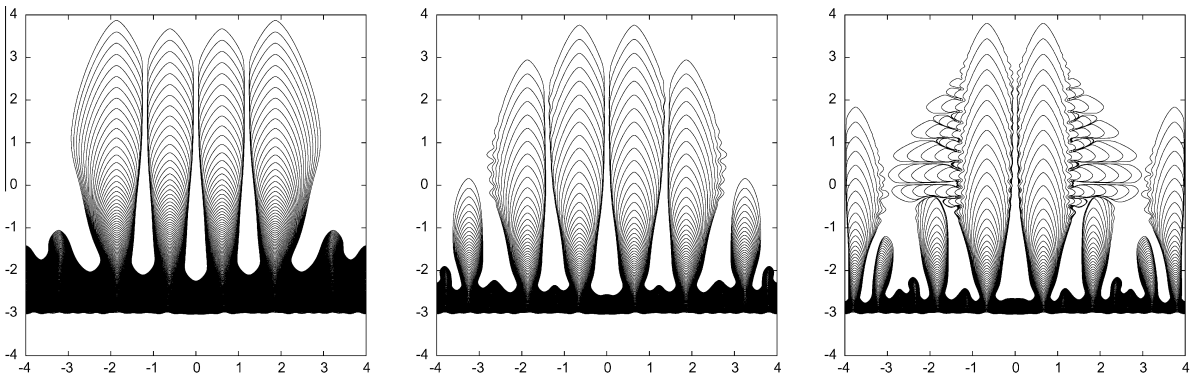

Fig. 8. $\vec{X}(t)$ at times $t = 0, 0.01, \ldots, \overline{T}$ with $\overline{T} = 1.42, 0.85, 0.63$ for $\mathcal{S} = 1$ and $\varsigma = 5 \times 10^{-3}$, 2×10^{-3}, 10^{-3}, respectively.

the solution u to (6.1a)–(6.1c), with u_D in (6.1b) replaced by $u|_{\partial_D\Omega}$, is given by

$$u(\vec{z},t) = \begin{cases} w(t) & |\vec{z}| \leqslant r(t), \\ w(t) + v\left(\frac{|\vec{z}|}{r(t)}\right) & |\vec{z}| > r(t). \end{cases} \tag{6.5}$$

For $d = 2$, we perform the following convergence experiment for the solution (6.5), where we set $\varsigma = \varrho = 10^{-3}$ and use $r(0) = R_0 = 0.5$. For $i = 0 \to 4$, we set $N_f = 2K_\Gamma^0 = 2^{7+i}$, $N_c = 4^i$ and $\tau = 4^{3-i} \times 10^{-3}$. The errors $\|U - I^h u\|_{L^\infty}$ and $\|\vec{X} - \vec{x}\|_{L^\infty}$ on the interval $[0, \overline{T}]$ with $\overline{T} = 1$, so that $r(\overline{T}) \approx 1.12$, are displayed in Table 1. Note that $K_\Gamma^M = 2K_\Gamma^0$ due to the growth of the interface.

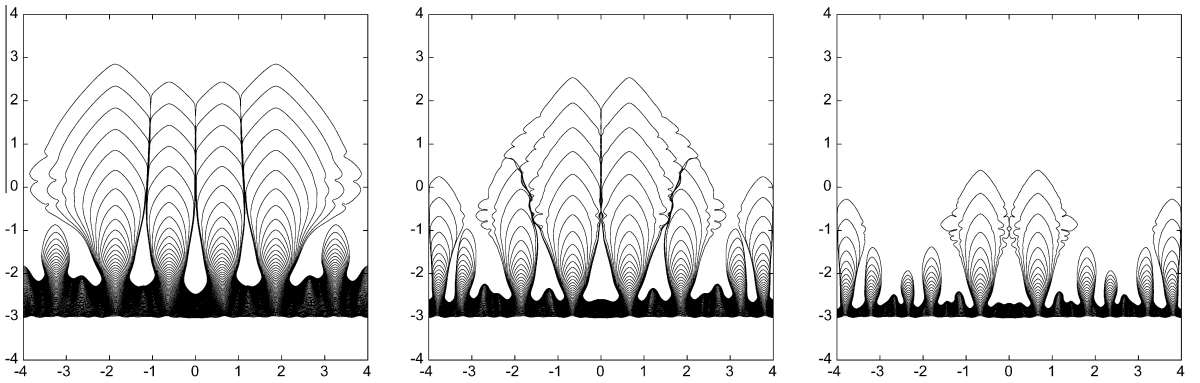

Fig. 9. $\vec{X}(t)$ at times $t = 0, 0.01, \ldots, \overline{T}$ with $\overline{T} = 0.63, 0.42, 0.3$ for $\mathcal{S} = \frac{5}{4}$ and $\varsigma = 5 \times 10^{-3}$, 2×10^{-3}, 10^{-3}, respectively.

In addition, we use the convergence experiment in order to compare the different integration rules for the cross terms (3.6). See Table 2, where we present the same computations as in Table 1, but now for (3.6)(i) and (ii). As is to be expected, the errors for the vertex sampling (3.6)(i) are larger than for the other two quadrature rules (ii) and (iii), while the latter two methods produce very similar errors.

Similarly to Table 1, we perform a convergence test for the solution (6.5), now for $d = 3$, leaving all the remaining parameters fixed as before. To this end, for $i = 0 \to 3$, we set $N_f = 2^{6+i}, N_c = 4^i, K^0_\Gamma = K(i)$, where $(K(0), K(1), K(2), K(3)) = (770, 3074, 12290, 49154)$, and $\tau = 4^{3-i} \times 10^{-3}$. The errors $\|U - I^h u\|_{L^\infty}$ and $\|\vec{X} - \vec{x}\|_{L^\infty}$ on the interval $[0, \overline{T}]$ with $\overline{T} = 0.1$, so that $r(\overline{T}) \approx 0.59$, are displayed in Table 3. Here $K^M_\Gamma = K^0_\Gamma$, as the interface has not grown sufficiently to merit a refinement as described in Section 5.2.

6.4. 2d results for the Stefan problem

In this subsection we use $\Omega = (-8,8)^2$ and set $\mathcal{S} = \frac{1}{2}, \varsigma = 5 \times 10^{-4}, \varrho = 10^{-2}$, unless otherwise stated. The initial interface is given by a circle of radius $R_0 = 0.05$.

For the anisotropy on the left of Fig. 2, we perform the following simulations, which highlight possible mesh effects that can be caused by numerical noise. Here we use three sets of discretization parameters. Let $N_f = 2^{9+i}$, $N_c = 2^{5+i}$, $K^0_\Gamma = 2^{4+i}$ and $\tau = 2^{1-2i} \times 10^{-3}$, $i = 0 \to 2$. The results are shown in Fig. 10, which indicate that the side branching observed in the experiment with the coarsest discretization parameters is simply due to numerical noise.

We repeat the experiments in Fig. 10 for the sixfold anisotropy on the right of Fig. 2. The results are shown in Fig. 11, where once again we observe that the sidebranching disappears once the discretization parameters are chosen fine enough. In summary we note that the sidebranching observed in Figs. 10 and 11 is caused by numerical noise, which is then amplified

Table 1
$\Omega = (-4,4)^2$ and $\overline{T} = 1$. Convergence test for (6.5) with (3.6)(iii).

h_f	h^M_Γ	$\|U - I^h u\|_{L^\infty}$	$\|\vec{X} - \vec{x}\|_{L^\infty}$	K^M_Ω	K^M_Γ
6.2500e−02	6.0083e−02	6.7004e−02	1.2155e−01	749	128
3.1250e−02	2.8906e−02	2.8054e−02	6.6655e−02	1321	256
1.5625e−02	1.4375e−02	1.4997e−02	3.2719e−02	2909	512
7.8125e−03	7.0224e−03	4.8878e−03	1.0036e−02	8945	1024
3.9062e−03	3.4677e−03	1.6308e−03	2.3839e−03	74597	2048

Table 2
$\Omega = (-4,4)^2$ and $\overline{T} = 1$. Convergence test for (6.5) with (3.6)(i) and (ii).

h_f	(3.6)(i)		(3.6)(ii)	
	$\|U - I^h u\|_{L^\infty}$	$\|\vec{X} - \vec{x}\|_{L^\infty}$	$\|U - I^h u\|_{L^\infty}$	$\|\vec{X} - \vec{x}\|_{L^\infty}$
6.2500e−02	6.6844e−02	1.2505e−01	6.7038e−02	1.2733e−01
3.1250e−02	3.2438e−02	8.4950e−02	2.7908e−02	6.6561e−02
1.5625e−02	1.6191e−02	3.8031e−02	1.4995e−02	3.2526e−02
7.8125e−03	5.1953e−03	1.0749e−02	4.8702e−03	9.9904e−03
3.9062e−03	1.6902e−03	2.5142e−03	1.6310e−03	2.3741e−03

Table 3
$\Omega = (-4,4)^3$ and $\overline{T} = 0.1$. Convergence test for (6.5) with (3.6)(iii).

h_f	h_Γ^M	$\|U - I^h u\|_{L^\infty}$	$\|\vec{X} - \vec{x}\|_{L^\infty}$	K_Ω^M	K_Γ^M
1.2500e−01	1.2341e−01	5.8883e−02	3.2225e−02	1781	770
6.2500e−02	6.2306e−02	1.7987e−02	1.5276e−02	6313	3074
3.1250e−02	3.1290e−02	9.0387e−03	8.1044e−03	26437	12290
1.5625e−02	1.5629e−02	5.3492e−03	4.1915e−03	358245	49154

due to the instability considered in Section 6.2. In situations where the modelling of sidebranching is important and desired, sidebranching can easily be achieved by adding random fluctuations to the model. This can be done e.g. for the temperature field, for the Gibbs–Thomson law or directly for the interface approximation itself. We give an example for the latter approach in Fig. 12. For the anisotropy as in Fig. 10 and on the larger domain $\Omega = (-16,16)^2$, we choose $\mathcal{S} = \frac{1}{2}$, $\varsigma = 10^{-3}$ and $\varrho = 10^{-2}$. The discretization parameters are $N_f = 4096$, $N_c = 256$, $\tau = 1.25 \times 10^{-4}$ and $K_\Gamma^0 = 64$. The first plot in Fig. 12 shows the smooth growth of four main dendritic arms. When some random noise of maximal magnitude 0.02 is added to the discrete interface Γ^m at time $t = 4$, this new evolution shows a pronounced sidebranching at later times.

6.5. 3d results for the Stefan problem

In this subsection, we let $\Omega = (-4,4)^3, \mathcal{S} = \frac{1}{2}$, $\varsigma = 10^{-3}$, $\varrho = 10^{-2}$ and let $\Gamma(0)$ be given by a sphere with radius $R_0 = 0.1$, unless otherwise stated.

The first experiment is for the anisotropy on the right of Fig. 3, but here with $\varepsilon = 0.6$. This anisotropy has what is sometimes called a cubic symmetry, and this will lead to the growth of dendrites with six main branches. First, similarly to Fig. 10, we numerically investigate the possible effects of rounding errors. To this end, we perform the following set of experiments. Let $N_f = 2^{7+i}$, $N_c = 2^{3+i}$, $J_\Gamma^0 = 3 \times 2^{6+i}$ and $\tau = 2^{5-2i} \times 10^{-4}$, $i = 0 \to 2$. The results are shown in Fig. 13. Once again we observe

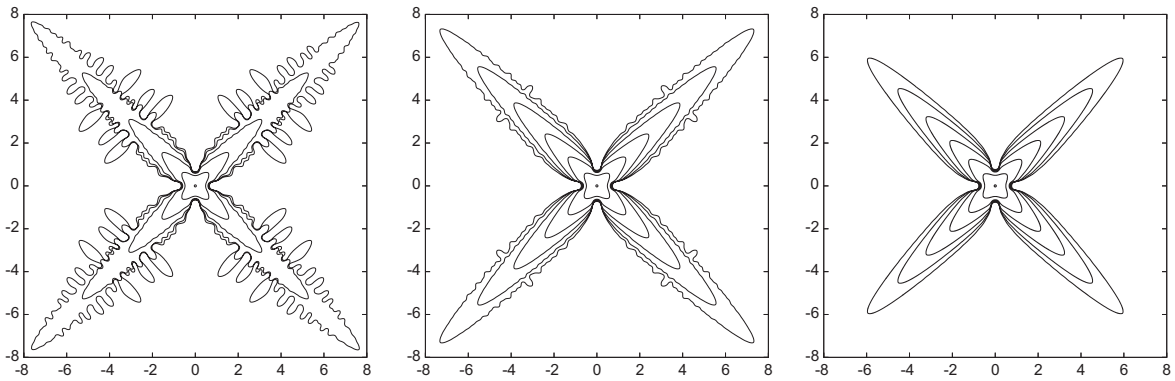

Fig. 10. $\vec{X}(t)$ for $t = 0, 0.5, \ldots, \overline{T}$ with $\overline{T} = 2.5, 3, 3$. Parameters are $N_f = 2^{9+i}, N_c = 2^{5+i}, K_\Gamma^0 = 2^{4+i}$ and $\tau = 2^{1-2i} \times 10^{-3}$, $i = 0 \to 2$.

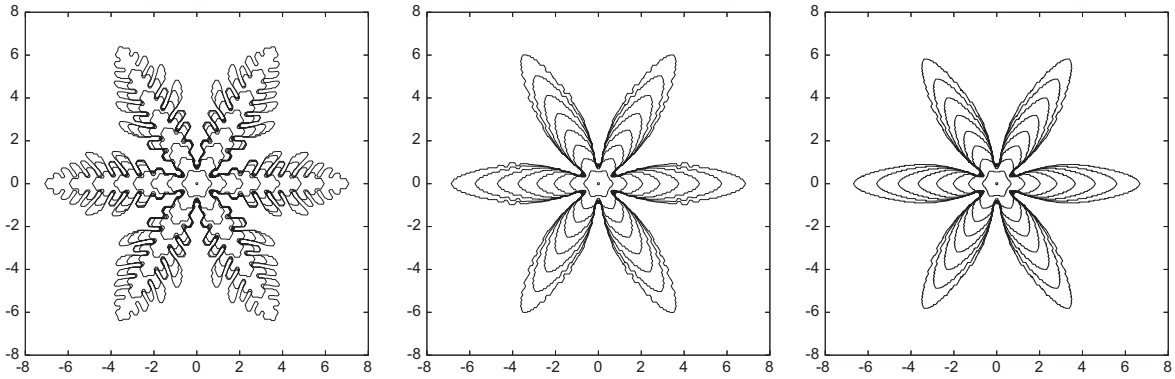

Fig. 11. $\vec{X}(t)$ for $t = 0, 0.5, \ldots, 4$. Parameters are $N_f = 2^{9+i}, N_c = 2^{5+i}, K_\Gamma^0 = 2^{4+i}$ and $\tau = 2^{1-2i} \times 10^{-3}$, $i = 0 \to 2$.

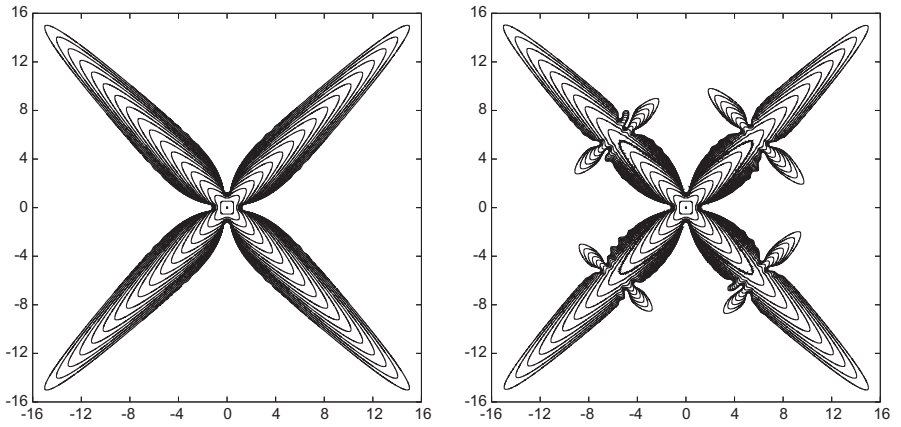

Fig. 12. $\vec{X}(t)$ for $t = 0, 0.5, \ldots, 9$. On the right the same evolution with random noise added to $\vec{X}(4)$.

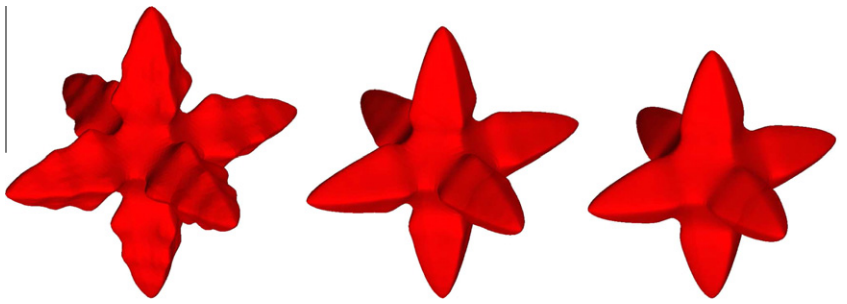

Fig. 13. $\vec{X}(0.25)$ for the following sets of parameters: $N_f = 2^{7+i}, N_c = 2^{3+i}, J_\Gamma^0 = 3 \times 2^{6+i}$ and $\tau = 2^{5-2i} \times 10^{-4}$, $i = 0 \to 2$.

that the oscillations and secondary sidebranching observed in the experiment for the coarsest set of discretization parameters is caused by numerical noise. The oscillations disappear once the discretization parameters are chosen sufficiently fine. More details of the finest computation in Fig. 13 are shown in Fig. 14. Here we observe the well-known growth from a spherical seed to a dendrite with six symmetric branches.

For the hexagonal anisotropy, as shown on the left of Fig. 3, we have the following results. We remark that such an anisotropy is understood to be the main driving force for the growth of snow crystals. Hence the numerical results presented here can be used to simulate such growth when we interpret (2.1a)–(2.1e) as a model for solidification from a supersaturated solution. See [40, Fig. 2] for a diagram on the different types of snow flakes.

For later use, we define the mobility:

$$\beta_{flat}(\vec{p}) := \left[p_1^2 + p_2^2 + \delta p_3^2\right]^{\frac{1}{2}} \tag{6.6}$$

with $\delta = 10^{-4}$. An experiment where initially we see "solid plates", recall [40, Fig. 2], is shown in Fig. 15. Here we used the anisotropy on the left of Fig. 3, but for this experiment set $\varepsilon = 10^{-2}$ in order to produce sharper polyhedrons. We also have

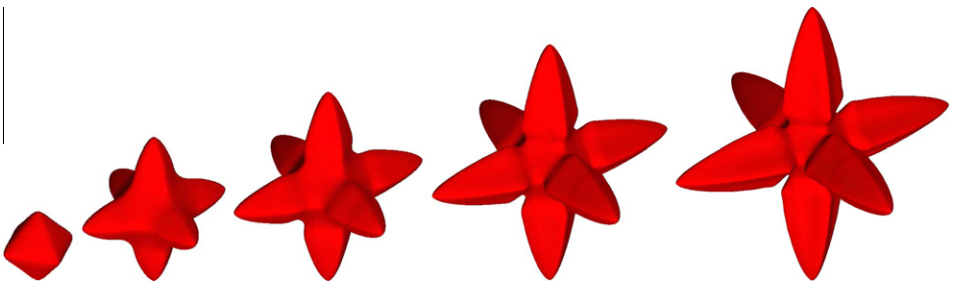

Fig. 14. $\vec{X}(t)$ at times $t = 0.1, 0.2, 0.25, 0.3, 0.34$.

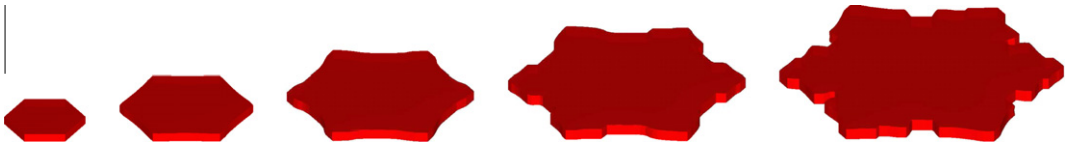

Fig. 15. $\vec{X}(t)$ for $t = 0.2, 0.3, 0.4, 0.5, 0.6$. $\varsigma = 2 \times 10^{-3}$, $\varrho = 10^{-2}$.

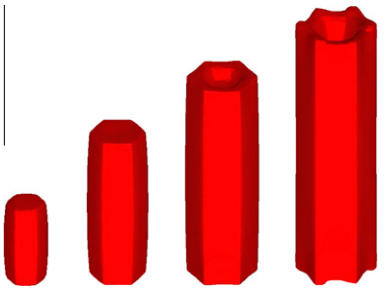

Fig. 16. $\vec{X}(t)$ for $t = 0.1, 0.2, 0.3, 0.4$ for $\beta = \beta_{tall}$.

$\beta = \beta_{flat}$ and here $\varsigma = 2 \times 10^{-3}$. The discretization parameters are $N_f = 128$, $N_c = 16$, $\tau = 10^{-3}$ and $K_\Gamma^0 = 98$. We observe that the corners of the solid plates soon become sharper and then develop something resembling "sectored plates"; see [40, Fig. 2].

Next we tried to produce the "hollow columns" from [40, Fig. 2]. To this end, we set $\beta = \beta_{tall}$, where

$$\beta_{tall}(\vec{p}) := [\delta p_1^2 + \delta p_2^2 + p_3^2]^{\frac{1}{2}}$$

with $\delta = 0.01$, and let $\varsigma = 10^{-3}$. The anisotropy γ is chosen as on the left of Fig. 3, while the discretization parameters are as before. The evolution of the interface for this experiment can be seen in Fig. 16, where we can observe the expected growth.

The next run is on the larger domain $\Omega = (-8,8)^3$ and an initial sphere with radius $R_0 = 0.05$. The discretization parameters are $N_f = 256$, $N_c = 32$, $\tau = 5 \times 10^{-4}$ and $K_\Gamma^0 = 98$. The anisotropy γ is as on the left of Fig. 3. A run for $\beta = \gamma\beta_{flat}$, and the latter defined by (6.6) with $\delta = 10^{-2}$, is shown in Fig. 17, where the upper and lower parts start to overgrow at around time $t = 0.23$. The shapes shown in Fig. 17 come very close to resembling real snow flakes. Here it should be noted, that the sidebranching observed there is very likely caused by numerical noise and rounding errors. However, the same effect, on even the most refined meshes, can be achieved by adding random fluctuations to the model, as discussed previously. In real life, such fluctuations and changes in physical parameters are experienced by the growing snow flake, as it moves through the atmosphere towards the earth.

Many mechanisms in snow crystal growth are still not fully understood. Experimentally it is observed that in a growing hexagonal prism sometimes the upper and lower basal facets break, while at other times the prism facets break, see e.g. [33] and [32]. Both scenarios are observed in our numerical experiments, see Figs. 16 and 17. Further numerical experiments are needed to obtain a better understanding of the governing mechanisms for facet breaking.

6.6. Convergence experiment for Mullins–Sekerka

Here we perform test computations for a well-known analytic solutions for the two phase Mullins–Sekerka problem (6.3a)–(6.3c) in the case of an isotropic surface energy (2.3). Here $\mathcal{S} = \varsigma = 1$ with $\partial_N\Omega = \partial\Omega$. In addition, $\Gamma(0)$ consists of two concentric spheres. It is then not difficult to show, that the two radii $r_1 < r_2$ satisfy the following system of nonlinear ODEs: In the case $d = 2$ we have:

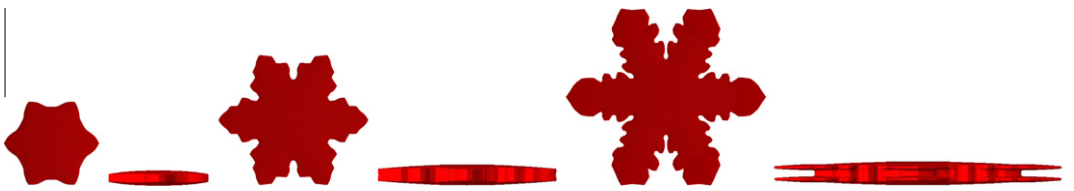

Fig. 17. $\vec{X}(t)$ for $t = 0.15, 0.22, 0.26$ for $\beta = \gamma\beta_{flat}$, $\delta = 0.01$.

$$[r_1]_t = -\frac{1}{r_1}\frac{\frac{1}{r_1}+\frac{1}{r_2}}{\ln\frac{r_2}{r_1}} \quad \text{and} \quad [r_2]_t = -\frac{1}{r_2}\frac{\frac{1}{r_1}+\frac{1}{r_2}}{\ln\frac{r_2}{r_1}} = \frac{r_1}{r_2}[r_1]_t \quad \forall\ t\in[0,\overline{T}_0), \tag{6.7a}$$

while for $d=3$ it holds that:

$$[r_1]_t = -\frac{2}{r_1^2}\frac{r_1+r_2}{r_2-r_1} \quad \text{and} \quad [r_2]_t = -\frac{2}{r_2^2}\frac{r_1+r_2}{r_2-r_1} = \frac{r_1^2}{r_2^2}[r_1]_t \quad \forall\ t\in[0,\overline{T}_0), \tag{6.7b}$$

where $\overline{T}_0$ is the extinction time of the smaller sphere, i.e. $\lim_{t\to\overline{T}_0} r_1(t)=0$, see e.g. [14] and [56], where we note that our definition of the mean curvature $\varkappa_\gamma \equiv \varkappa$ leads to a factor 2 in (6.7b) compared to [56]. Note that the corresponding solution u satisfying (2.1a)–(2.1e) is given by the radially symmetric function:

$$u(\vec{z},t) = \begin{cases} -\frac{d-1}{r_2(t)} & |\vec{z}| \geqslant r_2(t),\\ \begin{cases} \frac{1}{r_1(t)} - \ln\frac{|\vec{z}|}{r_1(t)}\frac{\frac{1}{r_1(t)}+\frac{1}{r_2(t)}}{\ln\frac{r_2(t)}{r_1(t)}} & d=2,\\ -\frac{4}{r_2(t)-r_1(t)} + \frac{2}{|\vec{z}|}\frac{r_1(t)+r_2(t)}{r_2(t)-r_1(t)} & d=3, \end{cases} & r_1(t) \leqslant |\vec{z}| \leqslant r_2(t),\\ \frac{d-1}{r_1(t)} & |\vec{z}| \leqslant r_1(t). \end{cases} \tag{6.8}$$

It is easy to see from (6.8) that the normal velocity of Γ is given by

$$\mathcal{V}|_{\Gamma_i} = \begin{cases} (-1)^{i+1}\frac{1}{r_i}\frac{\frac{1}{r_1}+\frac{1}{r_2}}{\ln\frac{r_2}{r_1}} & d=2,\\ (-1)^{i+1}\frac{2}{r_i^2}\frac{r_1+r_2}{r_2-r_1} & d=3, \end{cases} \qquad i=1,2.$$

As (6.7a), (6.7b) does not appear to be analytically solvable, it needs to be integrated numerically to compute the solution $(r_1, r_2)(t)$, for $t\in[0,\overline{T}]$, where $\overline{T}<\overline{T}_0$. We note that as the enclosed volume is conserved, recall (2.14), it holds that:

$$M_d^{-1}\, vol(\Omega_s(t)) = r_2^d(t) - r_1^d(t) = r_2^d(0) - r_1^d(0) =: v_0 \quad \forall\ t \geqslant 0,$$

where $M_2=\pi$ and $M_3=\frac{4}{3}\pi$, and hence $r_2(t) = (v_0 + r_1^d(t))^{\frac{1}{d}}$. Altogether this yields the scalar ODE:

$$[r_1]_t = \begin{cases} -\frac{1}{r_1}\frac{\frac{1}{r_1}+\left(v_0+r_1^2\right)^{-\frac{1}{2}}}{\ln\frac{\left(v_0+r_1^2\right)^{\frac{1}{2}}}{r_1}} & d=2,\\ -\frac{2}{r_1^2}\frac{r_1+\left(v_0+r_1^3\right)^{\frac{1}{3}}}{\left(v_0+r_1^3\right)^{\frac{1}{3}}-r_1} & d=3, \end{cases} \qquad \forall\ t\in[0,\overline{T}_0). \tag{6.9}$$

One possibility is to integrate (6.7a), (6.7b) directly, with e.g. a Runge–Kutta scheme. However, as we need to evaluate $r_1(t)$ very accurately, we employ the following approach. It follows from (6.9) that:

$$0 = t + \begin{cases} \int_{r_1(0)}^{r_1(t)} r\frac{\ln\frac{\left(v_0+r^2\right)^{\frac{1}{2}}}{r}}{\frac{1}{r}+\left(v_0+r^2\right)^{-\frac{1}{2}}}\,dr & d=2,\\ \int_{r_1(0)}^{r_1(t)} \frac{r^2}{2}\frac{\left(v_0+r^3\right)^{\frac{1}{3}}-r}{r+\left(v_0+r^3\right)^{\frac{1}{3}}}\,dr & d=3, \end{cases} \qquad \forall\ t\in[0,\overline{T}_0). \tag{6.10}$$

Now a simple root finding algorithm can be used to find $r_1(t)$ solving (6.10), and we employ the secant method. Here the integrals in (6.10) are evaluated using the Romberg method.

For the initial radii $r_1(0)=2$, $r_2(0)=3$ and the time interval $[0,\overline{T}]$ with $\overline{T}=1$, so that $r_1(\overline{T})\approx 0.69$ and $r_2(\overline{T})\approx 2.34$, we performed a convergence experiment for the true solution (6.8), at first for $d=2$. To this end, for $i=0\to 4$, we set $N_f = \frac{1}{2}K_\Gamma^0 = 2^{7+i}$, $N_c = 4^i$ and $\tau = 4^{3-i}\times 10^{-3}$. The errors $\|U - I^h u\|_{L^\infty}$ and $\|\vec{X}-\vec{x}\|_{L^\infty}$ on the interval $[0,\overline{T}]$ with $\overline{T}=1$ are displayed in Table 4. Note that, because the two circles are shrinking, it holds that $K_\Gamma^M = K_\Gamma^0$. In addition, we repeat the same convergence experiment for the two other integration rules for the cross terms in (3.6). See Table 5, where we present

Table 4
$\Omega = (-4,4)^2$ and $\overline{T}=1$. Convergence test for (6.8) with (3.6)(iii).

h_f	h_Γ^M	$\|U-I^h u\|_{L^\infty}$	$\|\vec{X}-\vec{x}\|_{L^\infty}$	K_Ω^M	K_Γ^M
6.2500e−02	1.1539e−01	3.3312e−01	7.8506e−02	2173	256
3.1250e−02	5.7439e−02	1.2935e−01	1.2009e−02	3841	512
1.5625e−02	2.8694e−02	1.8813e−02	6.2882e−03	7341	1024
7.8125e−03	1.4354e−02	4.6795e−03	4.7455e−03	17201	2048

Table 5
$\Omega = (-4,4)^2$ and $\overline{T} = 1$. Convergence test for (6.8) with (3.6)(i) and (ii).

h_f	(3.6)(i)		(3.6)(ii)	
	$\|U - I^h u\|_{L^\infty}$	$\|\vec{X} - \vec{x}\|_{L^\infty}$	$\|U - I^h u\|_{L^\infty}$	$\|\vec{X} - \vec{x}\|_{L^\infty}$
6.2500e−02	3.3802e−01	8.3705e−02	3.3312e−01	7.8507e−02
3.1250e−02	1.3288e−01	1.4938e−02	1.2935e−01	1.2009e−02
1.5625e−02	2.2092e−02	4.6987e−03	1.8812e−02	6.2882e−03
7.8125e−03	3.1831e−03	3.9429e−03	4.6796e−03	4.7455e−03

Table 6
$\Omega = (-4,4)^3$ and $\overline{T} = 0.1$. Convergence test for (6.8) and (3.6)(iii).

h_f	h_Γ^M	$\|U - I^h u\|_{L^\infty}$	$\|\vec{X} - \vec{x}\|_{L^\infty}$	K_Ω^M	K_Γ^M
2.5000e−01	6.0187e−01	3.0964e−01	2.0736e−02	11151	1540
1.2500e−01	3.0249e−01	1.1705e−01	1.1644e−02	44145	6148
6.2500e−02	1.5152e−01	4.8849e−02	6.8054e−03	175465	24580
3.1250e−02	7.5809e−02	2.1904e−02	3.5880e−03	900169	98308

the same computations as in Table 4, but now for (3.6)(i) and (ii). Here no clear conclusion is possible, apart from the fact that the errors for (3.6)(ii) and (iii) are very similar.

Similarly to Table 4, for the initial radii $r_1(0) = 2$, $r_2(0) = 3$ and the time interval $[0, \overline{T}]$ with $\overline{T} = 0.1$, so that $r_1(\overline{T}) \approx 1.74$ and $r_2(\overline{T}) \approx 2.90$, we performed a convergence experiment for the true solution (6.8) for $d = 3$. To this end, for $i = 0 \to 3$, we set $N_f = 2^{5+i}$, $N_c = 4^i$, $\frac{1}{2} K_\Gamma^0 = K(i)$, where $(K(0), K(1), K(2), K(3)) = (770, 3074, 12290, 49154)$, and $\tau = 4^{3-i} \times 10^{-3}$. The errors $\|U - I^h u\|_{L^\infty}$ and $\|\vec{X} - \vec{x}\|_{L^\infty}$ on the interval $[0, \overline{T}]$ with $\overline{T} = 0.1$ are displayed in Table 6.

6.7. 2d results for Mullins–Sekerka

Similarly to the numerical simulations shown in [62], we present some results for growing and shrinking circular particles, at first for an isotropic surface energy, (2.3). For the simulation in Fig. 18, we let $\Gamma(0)$ be the union of three circles with

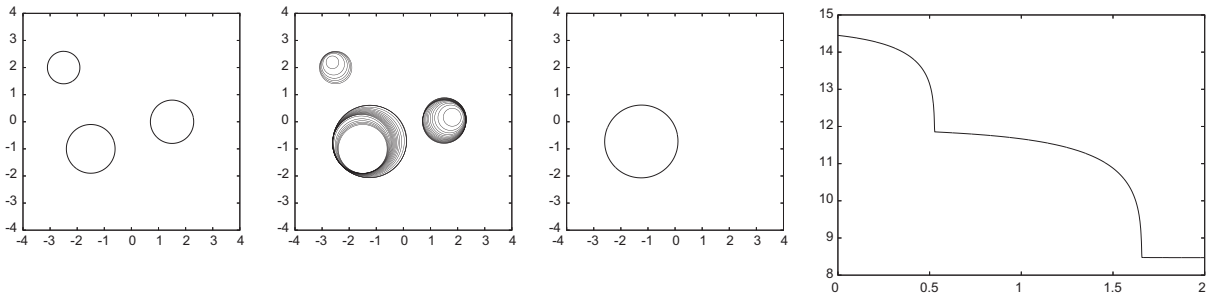

Fig. 18. $\vec{X}(t)$ at times $t = 0$, $t = 0, 0.1, \ldots, \overline{T} = 2$ and $t = \overline{T}$. On the right a plot of (6.11), i.e. $|\Gamma^m|$.

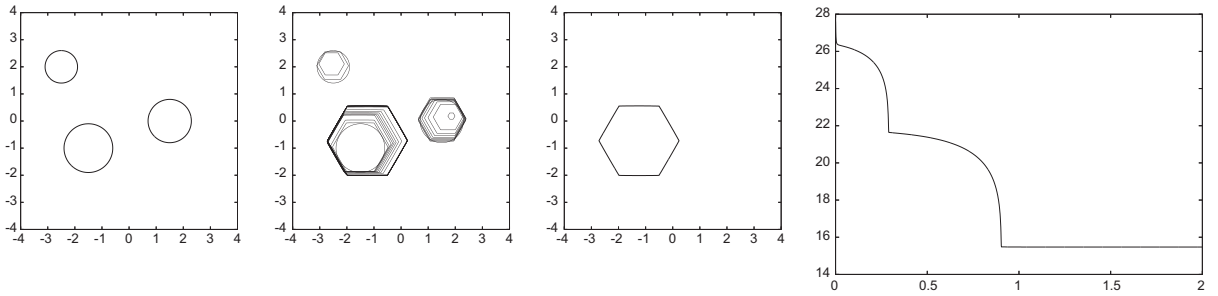

Fig. 19. $\vec{X}(t)$ at times $t = 0$, $t = 0, 0.1, \ldots, \overline{T} = 2$ and $t = \overline{T}$. On the right a plot of (6.11).

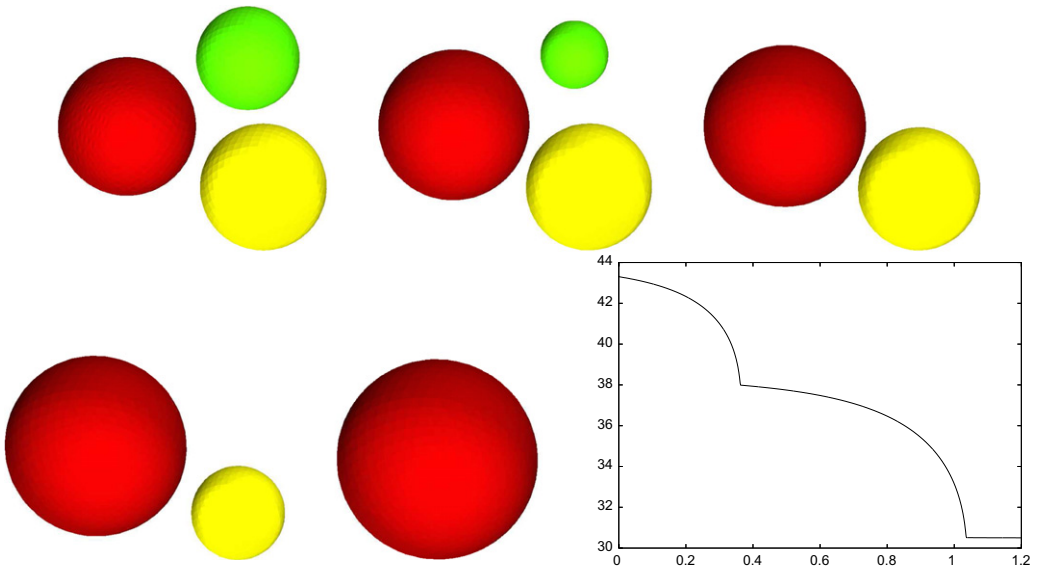

Fig. 20. $\vec{X}(t)$ at times $t = 0, 0.3, \ldots, \overline{T} = 1.2$. On the right, a plot of (6.11), i.e. $|\Gamma^m|$.

radii 0.6, 0.8 and 0.9. Under the Mullins–Sekerka flow, the two smaller circles shrink in size until they vanish, while the larger circle grows accordingly. Here we recall from (2.14) that the overall area/volume enclosed by Γ is conserved. Recall also that a single circular interface is a steady state solution. The shrinking and disappearing of the two smaller circles can clearly be seen in the plot of the discrete energy:

$$\widehat{\mathcal{E}}^m\left(\vec{X}^m\right) := \varsigma |\Gamma^m|_\gamma, \quad \text{with} \quad \varsigma = 1, \tag{6.11}$$

over time, which is also given in Fig. 18. The discretization parameters for this experiment are $N_f = 128$, $N_c = 16$, $\tau = 10^{-3}, \overline{T} = 2$ and $K_\Gamma^0 = 768$. We remark for the reader that a parametric approach cannot handle the vanishing of one of the particles, as this represents a singularity. Hence, for practical purposes, we discard a closed surface from the computations once its enclosed area/volume is smaller than 10^{-6}. The same simulation, but now with the anisotropic surface energy γ as on the right of Fig. 2, can be seen in Fig. 19.

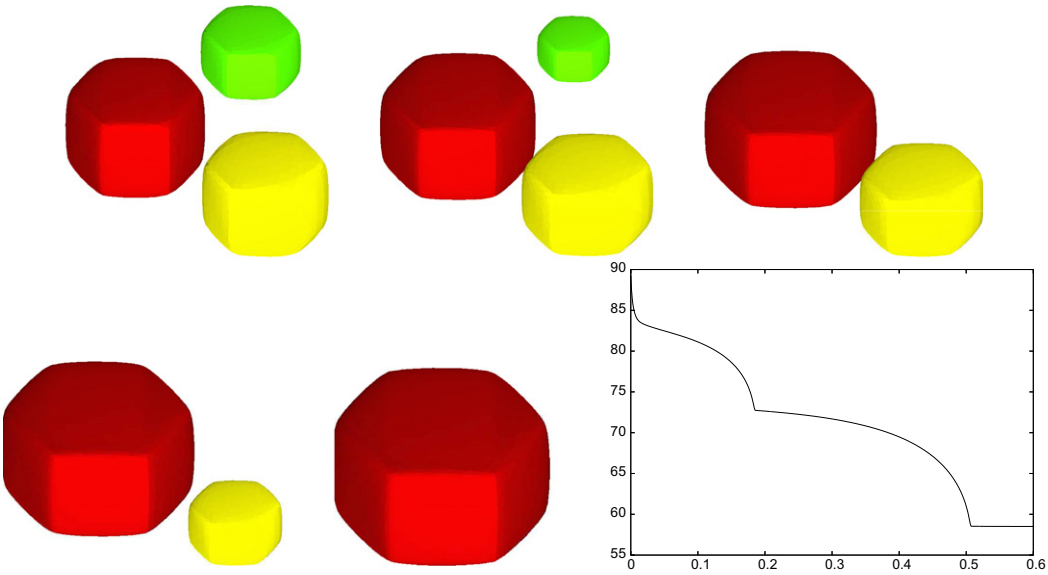

Fig. 21. $\vec{X}(t)$ at times $t = 0.05, 0.150.3, 0.45, \overline{T} = 0.6$. On the right, a plot of (6.11).

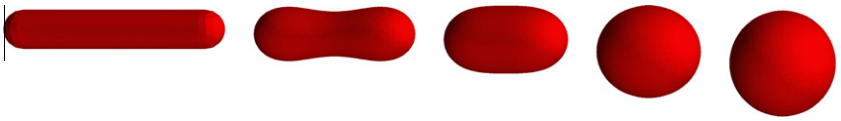

Fig. 22. $\vec{X}(t)$ at times $t = 0, 0.1, \ldots, \overline{T} = 0.4$.

6.8. 3d results for Mullins–Sekerka

Similarly to Fig. 18, we present some results for growing and shrinking particles, at first for an isotropic surface energy, (2.3). For the simulation in Fig. 20, we let $\Gamma(0)$ be the union of three spheres with radii 0.9, 1.1 and 1.2. As is to be expected, under the Mullins–Sekerka flow, the two smaller spheres shrink in size until they vanish, while the larger sphere grows accordingly. The shrinking and disappearing of the two smaller spheres can clearly be seen in the plot of the discrete energy (6.11) over time, which is also given in Fig. 20. The discretization parameters for this experiment are $N_f = 128, N_c = 16, \tau = 10^{-3}, \overline{T} = 0.4$ and $K^0_\Gamma = 2822$. The same evolution, but now for the anisotropic surface energy γ as shown on the left of Fig. 3, can be seen in Fig. 21. Here we observe that the three particles soon adopt a shape aligned with the Wulff shape of γ, before they shrink and expand similarly to the evolution in Fig. 20.

Finally, we also provide an evolution, in which an initially convex interface loses its convexity under the Mullins–Sekerka flow for an isotropic energy (2.3). Here we recall that the existence of such evolutions in the case $d = 2$ has been shown in [43]. In the experiment shown in Fig. 22, the initial surface $\Gamma(0)$ has total dimensions $6 \times 1 \times 1$. The discretization parameters for this computation are $N_f = 64$, $N_c = 8$, $\tau = 10^{-3}, \overline{T} = 0.4$ and $K^0_\Gamma = 358$. We observe that during the evolution the interface becomes nonconvex, before reaching a spherical steady state.

Appendix A. Discretizations for the Mullins–Sekerka problem as gradient flows

The Mullins–Sekerka problem with Neumann boundary conditions, i.e. problem (2.1a)–(2.1e) with:

$$\vartheta = \rho = f = 0, \tag{A.1a}$$

and (2.7)(ii), can be interpreted as a gradient flow for the surface energy $|\Gamma|_\gamma$. For simplicity we will, in this Appendix A, consider an isotropic surface energy (2.3) and set:

$$\beta = \mathcal{K} = \lambda = \alpha = a = 1. \tag{A.1b}$$

But we note that several generalizations are straightforward. We also refer to [44], where a gradient flow structure was used to derive discretizations of the Mullins–Sekerka problem in a way which is different to our approach.

A.1. The continuous gradient flow

In order to define a gradient flow one needs to introduce an inner product. For the Mullins–Sekerka problem one has to use a (volume based) H^{-1}-inner product in contrast to the H^{-1}-inner product on the surface Γ itself. Here we recall that the latter inner product gives rise to the well-known gradient flow called surface diffusion, see e.g. [17] and [10]. For the smooth reference manifold Υ and a given constant V_0, we define:

$$\mathcal{M} := \left\{ \vec{z} \in C^1(\Upsilon, \mathbb{R}^d) : \vec{z}(\Upsilon) \subset \Omega \text{ encloses a set with volume } V_0 \right\}.$$

Let $\vec{x} \in \mathcal{M}$ and let $\Gamma := \vec{x}(\Upsilon)$. Possible variations $\vec{x} : \Gamma \times (-\varepsilon_0, \varepsilon_0) \to \mathbb{R}^d$ of Γ with $\vec{x}(0) = \mathrm{i}\vec{\mathrm{d}}$ that maintain the enclosed volume fulfil $\int_\Gamma \partial_\varepsilon \vec{x}(0) \cdot \vec{\nu}\, ds = 0$. Hence we obtain that:

$$T_{\vec{x}}\mathcal{M} := \left\{ \vec{\eta} : \Gamma \to \mathbb{R}^d : \int_\Gamma \vec{\eta} \cdot \vec{\nu}\, ds = 0 \right\},$$

as the tangent space of $\mathcal{M}$. For later use we define the first variation of $|\Gamma|$ in the direction $\vec{\eta} \in T_{\vec{x}}\mathcal{M}$. Therefore we choose a family of surfaces parameterized by $\vec{x} : \Gamma \times (-\varepsilon_0, \varepsilon_0) \to \mathbb{R}^d, \varepsilon_0 > 0$, such that $\vec{x}(0) = \mathrm{i}\vec{\mathrm{d}}$, $\partial_\varepsilon \vec{x}(0) = \vec{\eta}$ and set:

$$\delta[|\Gamma(0)|](\vec{\eta}) = \frac{d}{d\varepsilon} |\Gamma(\varepsilon)|\big|_{\varepsilon=0} \quad \text{with} \quad \Gamma(\varepsilon) := \vec{x}(\Gamma, \varepsilon).$$

For all $\vec{\eta}, \vec{\xi} \in T_{\vec{x}}\mathcal{M}$ we define the H^{-1}-inner product:

$$\langle \vec{\eta}, \vec{\xi} \rangle_{-1} := \left(\nabla u_{\vec{\eta}}, \nabla u_{\vec{\xi}} \right), \tag{A.2}$$

where $u_{\vec{\eta}} \in H^1(\Omega)$ is defined such that:

$$(\nabla u_{\vec\eta},\nabla\phi)=\int_\Gamma \vec\eta\cdot\vec\nu\phi\ ds\quad\forall\ \phi\in H^1(\Omega),$$

and similarly for $u_{\vec\xi}\in H^1(\Omega)$. Existence of $u_{\vec\eta}$ and $u_{\vec\xi}$ follows because the solvability condition $\int_\Gamma \vec\eta\cdot\vec\nu\ ds=0$ holds. We remark that $u_{\vec\eta}$ and $u_{\vec\xi}$ are only unique up to an additive constant, but since only gradients enter into the definition of $\langle\cdot,\cdot\rangle_{-1}$, the inner product (A.2) is well-defined. In addition, we observe that:

$$\langle\vec\eta,\vec\xi\rangle_{-1}=\int_\Gamma(\vec\eta\cdot\vec\nu)u_{\vec\xi}\ ds=\int_\Gamma u_{\vec\eta}(\vec\xi\cdot\vec\nu)\ ds.$$

It is easy to see that the inner product $\langle\cdot,\cdot\rangle_{-1}$ is symmetric, bilinear and positive semi-definite. A solution $(\Gamma(t))_{t\geqslant0}$ to the H^{-1}-gradient flow equation for $|\Gamma|$ is now given as a solution of:

$$\delta[|\Gamma(t)|](\vec\eta)=-\langle\vec x_t,\vec\eta\rangle_{-1},\tag{A.3}$$

which has to hold for all $\vec\eta\in T_{\vec x}\mathcal{M}$, where $\vec x(t)$, as usual, parameterizes $\Gamma(t)$.

The definition (A.3) can be rewritten as

$$\langle\nabla_s\vec x,\nabla_s\vec\eta\rangle=-\int_{\Gamma(t)}u\vec\eta\cdot\vec\nu\ ds\quad\forall\quad\vec\eta\in T_{\vec x}\mathcal{M},\tag{A.4a}$$

where we recall the definition (2.10) and (2.12), and where $u\in H^1(\Omega)$ is such that:

$$(\nabla u,\nabla\phi)=\int_{\Gamma(t)}\vec x_t\cdot\vec\nu\phi\ ds\quad\forall\quad\phi\in H^1(\Omega).\tag{A.4b}$$

As discussed above, the function u is only defined up to a constant. Requiring that (A.4a) holds for all $\vec\eta:\Gamma\to\mathbb{R}^d$ fixes this constant without altering the evolving surfaces $(\Gamma(t))_{t\geqslant0}$, and hence we observe that (A.4a), (A.4b) and (2.8a)–(2.8c), with the assumptions stated in (A.1a), (A.1b), have the same solutions $(\Gamma(t))_{t\geqslant0}$.

A.2. The spatially discrete gradient flow

We now approximate Υ by a polyhedral surface Υ^h and define:

$$\mathcal{M}^h:=\left\{\vec\chi\in\underline{V}(\Upsilon^h):\vec\chi(\Upsilon^h)\subset\Omega\text{ encloses a set with volume }V_0\right\}.$$

Let $\vec X\in\mathcal{M}^h$ and let $\Gamma^h:=\vec X(\Upsilon^h)$. Then we define:

$$T_{\vec X}\mathcal{M}^h:=\left\{\vec\eta\in\underline{V}(\Gamma^h):\int_{\Gamma^h}\vec\eta\cdot\vec\nu^h\ ds=0\right\},$$

where $\vec\nu^h$ is a unit normal to Γ^h.

Introducing a finite element space S as in Remark 3.5, we can then define a discrete inner product for $\vec\eta,\vec\xi\in T_{\vec X}\mathcal{M}^h$ by

$$\left\langle\vec\eta,\vec\xi\right\rangle^h_{-1,h}:=\left(\nabla u^h_{\vec\eta},\nabla u^h_{\vec\xi}\right),$$

where $u^h_{\vec\eta}\in S$, and analogously $u^h_{\vec\xi}\in S$, are defined via:

$$\left(\nabla u^h_{\vec\eta},\nabla\varphi\right)=\langle\pi^h[\vec\eta\cdot\vec\omega^h],\varphi\rangle^\diamondsuit_h\quad\forall\ \varphi\in S,$$

where the discrete vertex normal $\vec\omega^h$ and the interpolation operator π^h are defined as in Remark 3.5. On recalling (3.15) we note that $\langle\pi^h[\vec\eta\cdot\vec\omega^h],1\rangle^\diamondsuit_h=\int_{\Gamma^h}\vec\eta\cdot\vec\nu^h\ ds=0$, which implies that (up to a constant) $u^h_{\vec\eta}$ and $u^h_{\vec\xi}$ are well-defined. The discrete gradient flow equation is now given as

$$\left\langle\nabla_s\vec X,\nabla_s\vec\eta\right\rangle_h=-\langle U,\pi^h[\vec\eta\cdot\vec\omega^h]\rangle^\diamondsuit_h\quad\forall\ \vec\eta\in T_{\vec X}\mathcal{M}^h,\tag{A.5a}$$

where $U\in S$ is defined by

$$(\nabla U,\nabla\varphi)=\left\langle\pi^h\left[\vec X_t\cdot\vec\omega^h\right],\varphi\right\rangle^\diamondsuit_h\quad\forall\quad\varphi\in S,\tag{A.5b}$$

and where $\vec X(t)$, as in Remark 3.5, parameterizes $\Gamma^h(t)$. If we require that (A.5a) holds for all test functions $\vec\eta\in\underline{V}(\Gamma^h)$, we obtain that $U\in S$ is unique. We remark that, for the stated choice of parameters (A.1a), (A.1b), the formulation (A.5a), (A.5b) is then equivalent to (3.14a)–(3.14c).

A.3. The fully discrete gradient flow

We now obtain our fully discrete scheme (3.5a)–(3.5c), for the choice of parameters (A.1a), (A.1b), if in (A.5a), (A.5b) we replace $\langle\cdot,\cdot\rangle_h^{(\diamond)}$ by $\langle\cdot,\cdot\rangle_m^{(\diamond)}$, $\vec{X}$ by $\vec{X}^{m+1}$, U by U^{m+1}, $\vec{\omega}^h$ by $\vec{\omega}^m$, π^h by π^m and $\vec{X}_t$ by $\frac{\vec{X}^{m+1}-\vec{X}^m}{\tau_m}$. In particular, given Γ^0, for $m = 0 \to M-1$, find $U^{m+1} \in S^m$ and $\vec{X}^{m+1} \in \underline{V}(\Gamma^m)$ such that:

$$\left(\nabla U^{m+1}, \nabla\varphi\right) = \left\langle \pi^m\left[\frac{\vec{X}^{m+1}-\vec{X}^m}{\tau_m}\cdot\vec{\omega}^m\right], \varphi\right\rangle_m^{\diamond} \quad \forall\ \varphi \in S^m, \tag{A.6a}$$

$$\left\langle \nabla_s\vec{X}^{m+1}, \nabla_s\vec{\eta}\right\rangle_m = -\left\langle U^{m+1}, \pi^m[\vec{\eta}\cdot\vec{\omega}^m]\right\rangle_m^{\diamond} \quad \forall\ \vec{\eta} \in \underline{V}(\Gamma^m). \tag{A.6b}$$

However, for the fully practical, semi-implicit approximation (A.6a), (A.6b) it does not appear possible to derive a gradient flow representation for the energy $|\Gamma|$ in a straightforward manner.

Hence we will first derive a gradient flow structure for the less practical, implicit and fully discrete scheme that is obtained by replacing $\langle\cdot,\cdot\rangle_m$ on the left-hand side of (A.6b) with $\langle\cdot,\cdot\rangle_{m+1}$. In a second step, we will show a gradient flow representation of (A.6a), (A.6b) for a quadratic approximation of the energy $|\Gamma|$.

To this end, we define a discrete inner product for $\vec{\eta}, \vec{\xi} \in \underline{V}_0(\Gamma^m) := \{\vec{\eta} \in \underline{V}(\Gamma^m) : \langle\vec{\eta}, \vec{\nu}^m\rangle_m = 0\}$ by

$$\left\langle \vec{\eta}, \vec{\xi}\right\rangle_{-1,m}^h := \left(\nabla U_{\vec{\eta}}^m, \nabla U_{\vec{\xi}}^m\right), \tag{A.7}$$

where $U_{\vec{\eta}}^m \in S$, and analogously $U_{\vec{\xi}}^m \in S$, are defined via:

$$(\nabla U_{\vec{\eta}}^m, \nabla\varphi) = \langle\pi^m[\vec{\eta}\cdot\vec{\omega}^m], \varphi\rangle_m^{\diamond} \quad \forall\ \varphi \in S.$$

We note that $\langle\pi^m[\vec{\eta}\cdot\vec{\omega}^m], 1\rangle_m^{\diamond} = \langle\vec{\eta}, \vec{\nu}^m\rangle_m = 0$, which implies that (up to a constant) $U_{\vec{\eta}}^m$ and $U_{\vec{\xi}}^m$ are well-defined. In addition, we introduce the norm $\|\cdot\|_{-1,m,h} = [\langle\cdot,\cdot\rangle_{-1,m}^h]^{\frac{1}{2}}$ induced by the H^{-1}-inner product (A.7) on Γ^m.

Then the implicit version of (A.6a), (A.6b) can be rewritten as the following minimization problem:

$$\vec{X}^{m+1} \in \arg\min_{\vec{X}\in\underline{V}(\Gamma^m)} \left[|\vec{X}(\Gamma^m)| + \frac{1}{2\tau_m}\|(\vec{X}-\vec{X}^m)\cdot\vec{\omega}^m\|_{-1,m,h}^2\right].$$

Our semi-implicit approximation (A.6a), (A.6b), on the other hand, can be rewritten as the following minimization problem:

$$\vec{X}^{m+1} \in \arg\min_{\vec{X}\in\underline{V}(\Gamma^m)} \left[\frac{1}{2}\int_{\Gamma^m}|\nabla_s\vec{X}|^2\ ds + \frac{1}{2\tau_m}\|(\vec{X}-\vec{X}^m)\cdot\vec{\omega}^m\|_{-1,m,h}^2\right].$$

Here we have made use of the quadratic approximation $\frac{1}{2}\int_{\Gamma^m}|\nabla_s\vec{X}|^2\ ds$ of the energy $|\vec{X}(\Gamma^m)|$, which for $d = 3$ is motivated by [8, Lemma 2.1] and which for $d = 2$ can be shown to be valid in a straightforward fashion. Finally, we stress that despite this substitution for the free energy term, the resulting scheme (A.6a), (A.6b) still mimics many features of the original gradient flow; e.g. it monotonically decreases the discrete free energy $|\Gamma^m|$, recall Theorem 3.2.

References

[1] R. Almgren, Variational algorithms and pattern formation in dendritic solidification, J. Comput. Phys. 106 (1993) 337–354.
[2] P.R. Amestoy, T.A. Davis, I.S. Duff, Algorithm 837: AMD, an approximate minimum degree ordering algorithm, ACM Trans. Math. Software 30 (2004) 381–388.
[3] L'. Baňas, R. Nürnberg, Finite element approximation of a three dimensional phase field model for void electromigration, J. Sci. Comput. 37 (2008) 202–232.
[4] J.W. Barrett, C.M. Elliott, A finite element method on a fixed mesh for the Stefan problem with convection in a saturated porous medium, in: K.W. Morton, M.J. Baines (Eds.), Numerical Methods for Fluid Dynamics, Academic Press, London, 1982, pp. 389–409.
[5] J.W. Barrett, C.M. Elliott, A finite-element method for solving elliptic equations with Neumann data on a curved boundary using unfitted meshes, IMA J. Numer. Anal. 4 (1984) 309–325.
[6] J.W. Barrett, H. Garcke, R. Nürnberg, A parametric finite element method for fourth order geometric evolution equations, J. Comput. Phys. 222 (2007) 441–462.
[7] J.W. Barrett, H. Garcke, R. Nürnberg, Numerical approximation of anisotropic geometric evolution equations in the plane, IMA J. Numer. Anal. 28 (2008) 292–330.
[8] J.W. Barrett, H. Garcke, R. Nürnberg, On the parametric finite element approximation of evolving hypersurfaces in $\mathbb{R}^3$, J. Comput. Phys. 227 (2008) 4281–4307.
[9] J.W. Barrett, H. Garcke, R. Nürnberg, A variational formulation of anisotropic geometric evolution equations in higher dimensions, Numer. Math. 109 (2008) 1–44.
[10] J.W. Barrett, H. Garcke, R. Nürnberg, Numerical approximation of gradient flows for closed curves in $\mathbb{R}^d$, IMA J. Numer. Anal. 30 (2010) 4–60.
[11] J.W. Barrett, H. Garcke, R. Nürnberg, Parametric approximation of surface clusters driven by isotropic and anisotropic surface energies, Interfaces Free Bound. 12 (2) (2010) 187–234.
[12] J.W. Barrett, R. Nürnberg, V. Styles, Finite element approximation of a phase field model for void electromigration, SIAM J. Numer. Anal. 42 (2004) 738–772.
[13] P.W. Bates, S. Brown, A numerical scheme for the Mullins–Sekerka evolution in three space dimensions, in: Differential Equations and Computational Simulations (Chengdu, 1999), World Scientific Publication, River Edge, NJ, 2000, pp. 12–26.
[14] P.W. Bates, X. Chen, X. Deng, A numerical scheme for the two phase Mullins–Sekerka problem, Electron. J. Differ. Equat. 1995 (1995) 1–28.

[15] E. Ben-Jacob, From snowflake formation to growth of bacterial colonies. Part I. Diffusive patterning in azoic systems, Contemp. Phys. 34 (1993) 247–273.
[16] W.J. Boettinger, J.A. Warren, C. Beckermann, A. Karma, Phase-field simulation of solidification, Annu. Rev. Mater. Res. 32 (2002) 163–194.
[17] J.W. Cahn, J.E. Taylor, Surface motion by surface diffusion, Acta Metall. Mater. 42 (1994) 1045–1063.
[18] L.Q. Chen, Phase-field models for microstructure evolution, Annu. Rev. Mater. Res. 32 (2002) 113–140.
[19] X. Chen, F. Reitich, Local existence and uniqueness of solutions of the Stefan problem with surface tension and kinetic undercooling, J. Math. Anal. Appl. 164 (1992) 350–362.
[20] S.H. Davis, Theory of Solidification, Cambridge Monographs on Mechanics, Cambridge University Press, Cambridge, 2001.
[21] T.A. Davis, Algorithm 832: UMFPACK V4.3 – an unsymmetric-pattern multifrontal method, ACM Trans. Math. Software 30 (2004) 196–199.
[22] T.A. Davis, Algorithm 849: a concise sparse Cholesky factorization package, ACM Trans. Math. Software 31 (2005) 587–591.
[23] K. Deckelnick, G. Dziuk, C.M. Elliott, Computation of geometric partial differential equations and mean curvature flow, Acta Numer. 14 (2005) 139–232.
[24] J. Duchon, R. Robert, Évolution d'une interface par capillarité et diffusion de volume. I. Existence locale en temps, Ann. Inst. Henri Poincare Anal. 1 (1984) 361–378.
[25] G. Dziuk, An algorithm for evolutionary surfaces, Numer. Math. 58 (1991) 603–611.
[26] C.M. Elliott, J.R. Ockendon, Weak and variational methods for moving boundary problems, Research Notes in Mathematics, vol. 59, Pitman (Advanced Publishing Program), Boston, MA, 1982.
[27] J. Escher, G. Simonett, Classical solutions for Hele–Shaw models with surface tension, Adv. Differ. Equat. 2 (1997) 619–642.
[28] I. Fonseca, S. Müller, A uniqueness proof for the Wulff theorem, Proc. R. Soc. Edinb. A 119 (1991) 125–136.
[29] M. Fried, A level set based finite element algorithm for the simulation of dendritic growth, Comput. Vis. Sci. 7 (2004) 97–110.
[30] M.J. Gander, C. Japhet, An algorithm for non-matching grid projections with linear complexity, in: M. Bercovier, M.J. Gander, R. Kornhuber, O. Widlund (Eds.), Domain Decomposition Methods in Science and Engineering XVIII, Springer-Verlag, 2009, pp. 185–192.
[31] H. Garcke, S. Schaubeck, Existence of weak solutions for the Stefan problem with anisotropic Gibbs–Thomson law, in preparation.
[32] T. Gonda, H. Gomi, Morphological instability of polyhedral ice crystals growing in air at low temperature, Ann. Glaciol. 6 (1985) 222–224.
[33] T. Gonda, T. Yamazaki, Morphological stability of polyhedral ice crystals growing from the vapor phase, J. Cryst. Growth 60 (1982) 259–263.
[34] M.E. Gurtin, Multiphase thermomechanics with interfacial structure. 1. Heat conduction and the capillary balance law, Arch. Ration. Mech. Anal. 104 (1988) 195–221.
[35] M.E. Gurtin, Thermomechanics of Evolving Phase Boundaries in the Plane, Oxford Mathematical Monographs, The Clarendon Press, Oxford University Press, New York, 1993.
[36] T.Y. Hou, J.S. Lowengrub, M.J. Shelley, Removing the stiffness from interfacial flows with surface tension, J. Comput. Phys. 114 (1994) 312–338.
[37] D. Juric, G. Tryggvason, A front-tracking method for dendritic solidification, J. Comput. Phys. 123 (1996) 127–148.
[38] R. Kobayashi, A numerical approach to three-dimensional dendritic solidification, Experiment. Math. 3 (1994) 59–81.
[39] J.S. Langer, Instabilities and pattern formation in crystal growth, Rev. Mod. Phys. 52 (1980) 1–28.
[40] K.G. Libbrecht, The physics of snow crystals, Rep. Prog. Phys. 68 (2005) 855–895.
[41] S. Luckhaus, Solutions for the two-phase Stefan problem with the Gibbs–Thomson law for the melting temperature, Eur. J. Appl. Math. 1 (1990) 101–111.
[42] S. Luckhaus, T. Sturzenhecker, Implicit time discretization for the mean curvature flow equation, Calc. Var. Partial Differ. Equat. 3 (1995) 253–271.
[43] U.F. Mayer, Two-sided Mullins–Sekerka flow does not preserve convexity, in: Proceedings of the Third Mississippi State Conference on Difference Equations and Computational Simulations (Mississippi State, MS, 1997), Southwest Texas State University, San Marcos, TX, 1998, Electron. J. Differ. Equat. Conf. 1 (1998) 171–179.
[44] U.F. Mayer, A numerical scheme for moving boundary problems that are gradient flows for the area functional, Eur. J. Appl. Math. 11 (2000) 61–80.
[45] W.W. Mullins, R.F. Sekerka, Morphological stability of a particle growing by diffusion or heat flow, J. Appl. Phys. 34 (1963) 323–329.
[46] W.W. Mullins, R.F. Sekerka, Stability of a planar interface during solidification of a dilute binary alloy, J. Appl. Phys. 35 (1964) 444–451.
[47] S. Osher, R. Fedkiw, Level set methods and dynamic implicit surfaces, Applied Mathematical Sciences, vol. 153, Springer-Verlag, New York, 2003.
[48] M. Röger, Existence of weak solutions for the Mullins–Sekerka flow, SIAM J. Math. Anal. 37 (2005) 291–301.
[49] A.R. Roosen, J.E. Taylor, Modeling crystal growth in a diffusion field using fully faceted interfaces, J. Comput. Phys. 114 (1994) 113–128.
[50] A. Schmidt, Die Berechnung dreidimensionaler Dendriten mit Finiten Elementen, Ph.D. Thesis, University Freiburg, Freiburg, 1993.
[51] A. Schmidt, Computation of three dimensional dendrites with finite elements, J. Comput. Phys. 195 (1996) 293–312.
[52] A. Schmidt, Approximation of crystalline dendrite growth in two space dimensions, in: Proceedings of the Algoritmy'97 Conference on Scientific Computing (Zuberec), Acta Math. Univ. Comenian. (N.S.), 67 (1998) 57–68.
[53] A. Schmidt, K.G. Siebert, Design of adaptive finite element software: the finite element toolbox ALBERTA, Lecture Notes in Computational Science and Engineering, vol. 42, Springer-Verlag, Berlin, 2005.
[54] J.A. Sethian, Level Set Methods and Fast Marching Methods, Cambridge University Press, Cambridge, 1999.
[55] I. Singer-Loginova, H.M. Singer, The phase field technique for modeling multiphase materials, Rep. Prog. Phys. 71 (2008) 106501. 32 p..
[56] B.E.E. Stoth, Convergence of the Cahn–Hilliard equation to the Mullins–Sekerka problem in spherical symmetry, J. Differ. Equat. 125 (1996) 154–183.
[57] A. Veeser, Stability of flat interfaces during semidiscrete solidification, M2AN Math. Model. Numer. Anal. 36 (2002) 573–595.
[58] A. Visintin, Models of phase transitions, Progress in Nonlinear Differential Equations and their Applications, vol. 28, Birkhäuser Boston Inc, Boston, MA, 1996.
[59] V.V. Voronkov, Conditions for formation of mosaic structure on a crystallization front (in Russian), Fiz. Tverd. Tela 6 (1964) 2984–2988.
[60] V.V. Voronkov, Conditions for formation of mosaic structure on a crystallization front, Sov. Phys. Solid State 6 (1965) 2378–2381.
[61] G. Wulff, Zur Frage der Geschwindigkeit des Wachstums und der Auflösung der Kristallflächen, Z. Kristallogr. 34 (1901) 449–530.
[62] J. Zhu, X. Chen, T.Y. Hou, An efficient boundary integral method for the Mullins–Sekerka problem, J. Comput. Phys. 127 (1996) 246–267.